Viscothermal models for wind musical instruments

Alexis Thibault, Juliette Chabassier

Viscothermal models for wind musical instruments.

Juliette Chabassier, Alexis Thibault

RESEARCH REPORT
N° 9356
March 2020
Project-Teams Magique 3d

ISSN 0249-6399 ISRN INRIA/RR--9356--FR+ENG

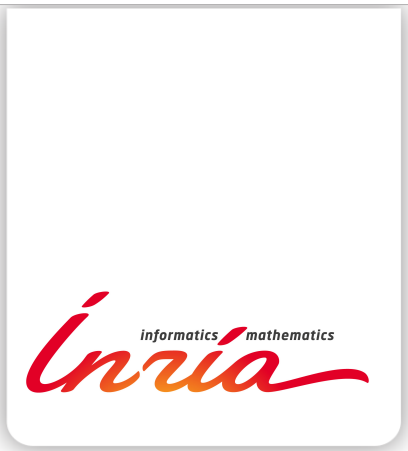

Viscothermal models for wind musical instruments.

Juliette Chabassier*†, Alexis Thibault*†

Project-Teams Magique 3d

Research Report n° 9356 — March 2020 — 31 pages

Abstract: This work focuses on thermal and viscous effects on linear wave propagation inside a pipe. It aims at understanding the ground on which are built many dissipative propagating wave models found in the musical acoustics literature, in order to quantify, as much as possible, the underlying assumptions and model errors which are performed. The Navier-Stokes (NS) equations, which are nonlinear and expressed in the 3 dimensions of space, are the starting point of all models. Thermoviscous (or viscothermal) equations are derived from NS equations mainly after linearization and assumptions on the gas state equation. Analytical or numerical solutions to these equations can be proposed, after modifying more of less the original system. These derived models are summed-up in a global sketch of the underlying hypotheses. What is observed is that the thermal and viscous effects are mainly confined near the boundaries of the pipe, in regions called "boundary layers", whose lengths depend on the physical coefficients and the harmonic regime. These thermal and viscous effects can therefore be neglected far from the boundaries (where a standard 3D Helmholtz wave equation holds). These procedures can lead to 3D models, describing the propagation of the pressure field in all the domain or only a part of it, or 1D models, describing the propagation of the mean pressure across a pipe section. Some other 1D models are obtained from derived 3D models, and describe the propagation of the pressure near the boundary layer. The time dependancy of these derived models can be very intricate because the model derivation is done in the harmonic regime, and nonlocal operators can arise. An additional modelling step can lead to local time-domain 1D models. An assessment of some of these 3D and 1D models is proposed, aiming at a quantitative estimation of the model errors with respect to their domains of validity, and at a comparison between some models for simple geometries.

Key-words: viscothermal boundary layers, linear acoustic wave propagation, pipe modelling, model error

* Magique 3d team, Inria Sud Ouest, 200 Avenue de la Vieille Tour, Talence, France.
† Laboratoire de Mathématiques et leurs Applications, Université de Pau et des Pays de l'Adour, Pau, France.

RESEARCH CENTRE
BORDEAUX – SUD-OUEST

200 Avenue de la Vieille Tour,
33405 Talence Cedex

Viscothermal models for wind musical instruments.

Résumé : Ce travail porte sur les effets visqueux et thermiques se manifestant lors de la propagation d'ondes linéaires dans un tuyau. Il vise à comprendre le fondement sur lequel s'appuient de nombreux modèles d'ondes dissipatives courants en acoustique musicale, afin de quantifier autant que possible, les hypothèses sous jacentes et les erreurs de modèle effectuées. Les équations de Navier-Stokes (NS), qui sont non linéaires et formulées dans les trois dimensions de l'espace, forment le point de départ de tous les modèles. Les équations thermovisqueuses (ou viscothermiques) sont dérivées des équations de NS essentiellement après une étape de linéarisation et certaines hypothèses sur l'équation d'état du gaz. Des solutions analytiques ou numériques peuvent être proposées, après des modifications plus ou moins profondes du système original. Ces modèles dérivés sont résumés dans un schéma global précisant les hypothèses effectuées. Ce que l'on peut observer est que les effets thermiques et visqueux sont essentiellement confinés à proximité des bords du tuyau, dans une région abritant les "couches limites", dont la taille caractéristique dépend des coefficients physiques et du régime harmonique. Ces effets thermiques et visqueux peuvent donc être négligés loin des bords (où une équation de Helmholtz 3D standard est valide). Ces procédures peuvent mener à l'établissement de modèles 3D qui décrivent la propagation du champ de pression dans tout le domaine ou seulement une sous partie, ou de modèles 1D qui décrivent la propagation de la pression moyenne sur une section du tuyau. D'autres modèles 1D peuvent découler des modèles 3D, et décrivent la propagation de la pression au voisinage des couches limites. La dépendance en temps de ces modèles dérivés est parfois très délicate car leur dérivation est faite dans le régime harmonique, faisant apparaitre des opérateurs non locaux. Une étape supplémentaire de modélisation peut aboutir à des modèles 1D locaux en temps. Ce travail propose une évaluation de certains de ces modèles (3D et 1D), à travers une estimation quantitative des erreurs de modèles en lien avec leurs domaines de validité, ainsi qu'une comparaison entre les modèles pour des géométries simples.

Mots-clés : couches limites viscothermiques, propagation d'ondes acoustiques linéaires, modélisation de tuyau, erreur de modèle

Contents

1 Motivations

This work focuses on thermal and viscous effects on linear wave propagation inside a pipe. It aims at understanding the ground on which are built many dissipative propagating wave models found in the musical acoustics literature, in order to quantify, as much as possible, the underlying assumptions and model errors which are performed. The Navier-Stokes (NS) equations, which are nonlinear and expressed in the 3 dimensions of space, are the starting point of all models. Thermoviscous (or viscothermal) equations are derived from NS equations mainly after linearization and assumptions on the gas state equation. Analytical or numerical solutions to these equations can be proposed, after modifying more of less the original system. These derived models are described in Sec. 2, and a global sketch of the underlying hypotheses is proposed in Fig. 1. What is observed is that the thermal and viscous effects are mainly confined near the boundaries of the pipe, in regions called "boundary layers", whose lengths depend on the physical coefficients and the harmonic regime. These thermal and viscous effects can therefore be neglected far from the boundaries (where a standard 3D Helmholtz wave equation holds). These procedures, described in Sec. 3, can lead to 3D models, describing the propagation of the pressure field in all the domain or only a part of it, or 1D models, describing the propagation of the mean pressure across a pipe section. Some other 1D models are obtained from derived 3D models, and describe the propagation of the pressure near the boundary layer. The time dependancy of these derived models can be very intricate because the model derivation is done in the harmonic regime, and nonlocal operators can arise. An additional modelling step can lead to local time-domain 1D models. These 1D models are described in Sec. 4. An assessment of some of these 3D and 1D models is proposed in Sec. 5, aiming at a quantitative estimation of the model errors with respect to their domains of validity, and at a comparison between some models for simple geometries.

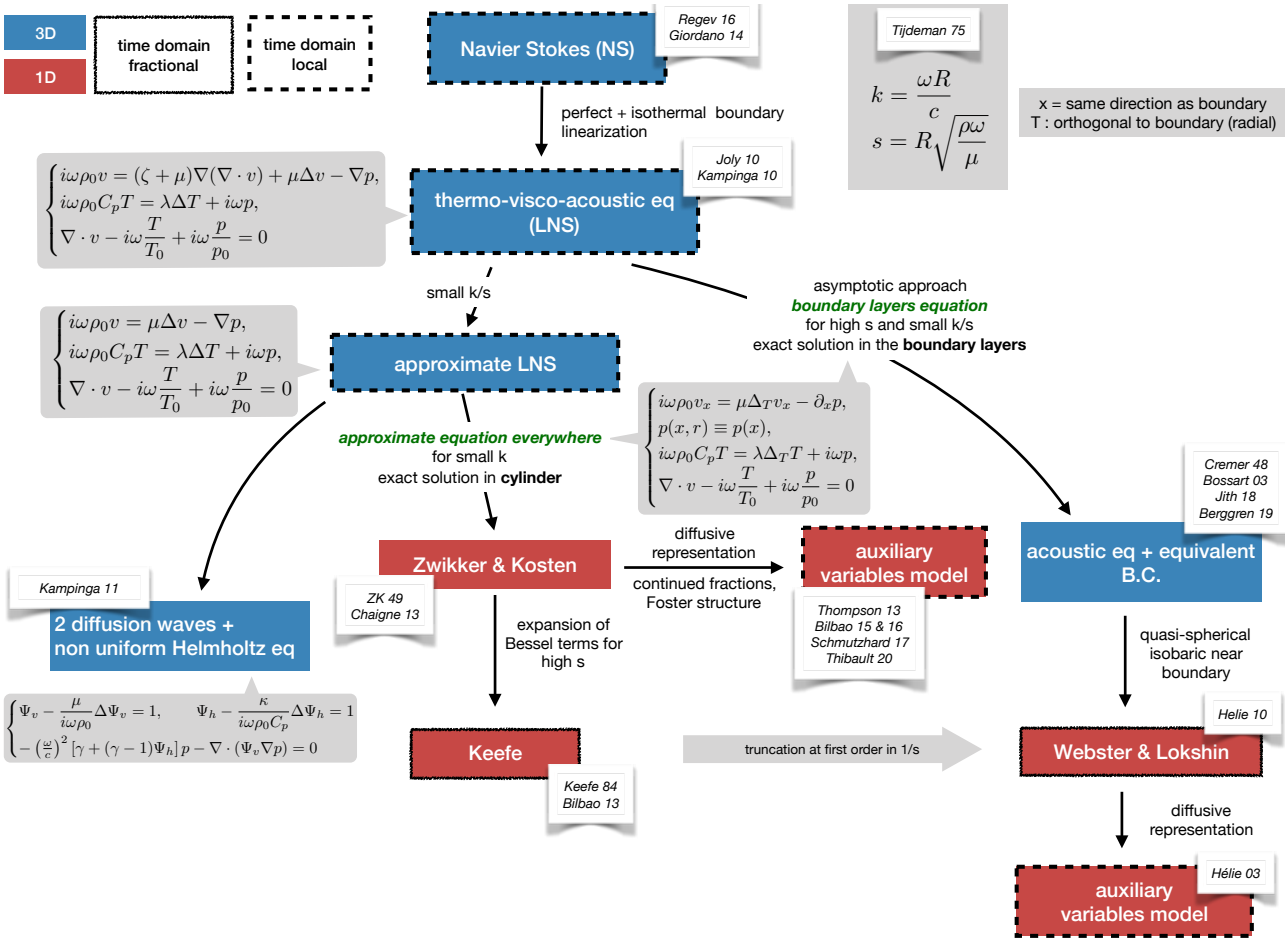

Figure 1: Derivation of some models for dissipative wind musical instruments with radius R and pulsation $\omega = 2\pi f$.

2 Thermoviscous equations

2.1 Derivation from Navier-Stokes equations

This section spells out the equations describing the dynamics of a gas, and their simplification into the Linearized Navier–Stokes (LNS) system, also called "thermoviscoacoustic equations".

We denote the gas's density field by ρ, its physical pressure by P, its velocity by $\boldsymbol{v}$, and its temperature by T. The general equations for the motion of a fluid are derived in [Regev et al., 2016]. They consist of:

- The Navier-Stokes equations of mass conservation and momentum conservation:

$$\partial_t \rho + \operatorname{div}(\rho \boldsymbol{v}) = 0, \tag{1a}$$

$$\rho \left[\partial_t \boldsymbol{v} + (\boldsymbol{v}\cdot\nabla)\boldsymbol{v}\right] = \rho f^{\text{ext}} - \nabla P + \mu \nabla^2 \boldsymbol{v} + \left(\zeta + \frac{1}{3}\mu\right)\nabla(\nabla\cdot\boldsymbol{v}). \tag{1b}$$

  where f^{ext} denotes the external forces, and the viscous forces have been expressed using the dynamic shear viscosity μ and bulk viscosity ζ.

- The energy equation[1] [Tijdeman, 1975]:

$$\rho C_p \left(\partial_t T + (\boldsymbol{v}\cdot\nabla)T\right) = -\nabla\cdot\boldsymbol{q} + \partial_t P + \sum_{i,k}\left(\boldsymbol{\tau}^{\text{vis}}_{ik}\frac{\partial v_k}{\partial x_i}\right), \tag{1c}$$

  where the viscous stress tensor $\boldsymbol{\tau}^{\text{vis}}$ is given by

$$\boldsymbol{\tau}^{\text{vis}}_{ik} = \mu\left[\frac{\partial v_i}{\partial x_k} + \frac{\partial v_k}{\partial x_i} - \frac{2}{3}\delta_{ik}\frac{\partial v_m}{\partial x_m}\right] + \zeta\delta_{ik}\frac{\partial v_m}{\partial x_m},$$

  and the heat flux $\boldsymbol{q}$ is given by Fourier's law, using the thermal conductivity coefficient λ:

$$\boldsymbol{q} = -\lambda\nabla T.$$

- An equation of state, linking the thermodynamic variables. We make the assumption that the considered gas is ideal [Tijdeman, 1975][2]:

$$P = \rho R_0 T. \tag{1d}$$

For acoustical purposes we make a number of simplifying hypotheses. The influence of gravity, which at rest is compensated by a vertical pressure gradient, is neglected by setting $f^{\text{ext}} = 0$. Bulk viscosity ζ, which is influential when considering shock wave phenomena, is also disregarded here and set to zero. All variables are assumed to remain close to the static equilibrium state of *air at rest*, so that the equations can be linearized. We denote $p, \rho_{ac}, \boldsymbol{v}_{ac}, T_{ac}$ the *acoustic part* of the unknowns[3], i.e. small variations around the equilibrium, and assume that there is no mean flow[4].

$$P = p_0 + p_{ac}, \tag{2a}$$

$$\rho = \rho_0 + \rho_{ac}, \tag{2b}$$

$$\boldsymbol{v} = 0 + \boldsymbol{v}_{ac}, \tag{2c}$$

$$T = T_0 + T_{ac}. \tag{2d}$$

Due to (1d) the static pressure, density and temperature are linked by $P_0 = \rho_0 R_0 T_0 = \dfrac{\rho_0 c_0^2}{\gamma}$. After linearization, equations (1a-1d) become :

$$\partial_t \rho_{ac} + \rho_0 \operatorname{div}\boldsymbol{v}_{ac} = 0, \tag{3a}$$

$$\rho_0 \partial_t \boldsymbol{v}_{ac} = -\nabla p_{ac} + \mu\left(\nabla^2\boldsymbol{v}_{ac} + \frac{1}{3}\nabla(\nabla\cdot\boldsymbol{v}_{ac})\right), \tag{3b}$$

$$\rho_0 C_p \partial_t T_{ac} = \lambda\nabla^2 T_{ac} + \partial_t p_{ac}, \tag{3c}$$

$$\frac{p_{ac}}{p_0} = \frac{\rho_{ac}}{\rho_0} + \frac{T_{ac}}{T_0}. \tag{3d}$$

[1] Other writings of the energy equation exist, expressed using internal energy per unit of mass [Regev et al., 2016] (1.51), or entropy [Bruneau, 2013] (2.40).

[2] It is possible to avoid this assumption by using a more general equation of state, see for example [Bruneau, 2013] (1.22).

[3] In [Tijdeman, 1975] a shifting and scaling of the unknowns is made, so as to nondimensionalize the equations. In the current document the acoustic variables $\cdot_{ac}$ are obtained only by shifting to the equilibrium point, as is more common in the acoustic literature [Bruneau, 2013].

[4] In the presence of a mean flow, a Doppler effect may appear [Bruneau, 2013] (10.114) depending on the Mach number. For music instruments the mean flow rarely exceeds a few meters per second, meaning the Mach number could reach at most a few percent. This effect is usually neglected.

Note that all terms of order 2 have been eliminated, including all convection terms, and the heat source due to viscosity. The system formed by equations (3a-3d) is here called "Linearized Navier–Stokes" (LNS), and forms the starting point of the derivation of more specialized models.

Remark 1. *It is possible to eliminate ρ from the previous equations, to obtain only three equations on $\boldsymbol{v}, T, p$ as is done in [Kampinga et al., 2010], and to eliminate also p in order to obtain only two equations on $\boldsymbol{v}, T$, as is done in [Joly, 2010].*

2.2 Viscothermal analytical solution in a cylinder

The Linearized Navier–Stokes system of equations can be solved analytically in some configurations, to obtain special solutions of (3). One such configuration is that of an infinite cylinder with a perfectly rigid isothermal wall. The system (3) must be solved with boundary conditions:

- Perfectly rigid wall: on the surface of the cylinder,

$$\boldsymbol{v}_{ac} = 0 \tag{4a}$$

- The heat conductivity of the tube wall is large compared to that of the fluid: on the surface of the cylinder,

$$T_{ac} = 0. \tag{4b}$$

Kirchhoff studied this problem and gave an exact solution for propagation at each frequency. Simplified solutions were later proposed, which can also be viewed as "exact solutions" of simplified equations [Zwikker and Kosten, 1949, Tijdeman, 1975].

As explained by Tijdeman, this problem can be described in terms of four significant parameters:

- $s = R\sqrt{\rho_0\omega/\mu}$ the shear wave number, sometimes also referred to as the Stokes number,
- $\dfrac{\omega R}{c}$ the reduced frequency, which Tijdeman denotes as k (but is not the wavenumber),
- $\sigma = \sqrt{\mu C_p/\lambda}$, the square root of the Prandtl number,
- $\gamma = C_p/C_v$ the ratio of specific heats.

For a given gas, σ and γ can be considered as constants, so that the two main parameters are the shear wave number s and the reduced frequency k. Kirchoff's solution is valid in all regimes, whereas the approximation by Zwikker and Kosten is valid for small reduced frequency.

2.2.1 Kirchhoff's solution

Let us recall the exact solution of Kirchhoff for propagation in a cylindrical tube [Kirchhoff, 1868] as formulated in [Stinson, 1991]. The exact study of (3) with boundary conditions (4) leads to an equation in which the wavenumber is given implicitly as the root of a complex function.

Stinson chooses to use two constants ν, ν' which he defines as :

$$\nu = \mu/\rho_0 = R^2\omega/s^2, \qquad \nu' = \lambda\gamma/(\rho_0 C_p) = R^2\omega\gamma/(\sigma^2 s^2). \tag{5}$$

Let the acoustic velocity be composed of axial (along x-component) and radial components:

$$\boldsymbol{v}_{ac} = v_x\hat{x} + v_r\hat{r}. \tag{6}$$

Then, traveling wave solutions are given by

$$v_x = mB\left[-j\omega\left(\frac{1}{\lambda_1} - \frac{1}{\lambda_2}Q_{1w}Q_{2w}Q + \left(\frac{j\omega}{\lambda_1} - \nu'\right)Q_wQ_{2w}Q_1 - \left(\frac{j\omega}{\lambda_2} - \nu'\right)Q_wQ_{1w}Q_2\right)\right]e^{mx}, \tag{7}$$

$$v_r = B\left[\frac{j\omega m^2}{(j\omega/\nu) - m^2}\left(\frac{1}{\lambda_1} - \frac{1}{\lambda_2}\right)Q_{1w}Q_{2w}\frac{\mathrm{d}Q}{\mathrm{d}r} + \left(\frac{j\omega}{\lambda_1} - \nu'\right)Q_wQ_{2w}\frac{\mathrm{d}Q_1}{\mathrm{d}r} - \left(\frac{j\omega}{\lambda_2} - \nu'\right)Q_wQ_{1w}\frac{\mathrm{d}Q_2}{\mathrm{d}r}\right], \tag{8}$$

$$T_{ac} = B(\gamma - 1)T_0Q_w(-Q_{2w}Q_1 + Q_{1w}Q_2)e^{mx}, \tag{9}$$

where the functions Q, Q_1, Q_2 are given by

$$Q = J_0\left[r\sqrt{m^2 - j\omega/\nu}\right], \tag{10}$$

$$Q_1 = J_0\left[r\sqrt{m^2 - \lambda_1}\right], \tag{11}$$

$$Q = J_0\left[r\sqrt{m^2 - \lambda_2}\right], \tag{12}$$

and where λ_1, λ_2 are the small and large roots of

$$\lambda^2\left(\frac{c^2\nu'}{j\omega\gamma} + \frac{4}{3}\nu\nu'\right) - \lambda\left[c^2 + j\omega\left(\frac{4}{3}\nu + \nu'\right)\right] - \omega^2 = 0. \tag{13}$$

The propagation constant m can be evaluated by solving numerically:

$$\frac{j\omega m^2}{(j\omega/\nu) - m^2}\left(\frac{1}{\lambda_1} - \frac{1}{\lambda_2}\right)\left.\frac{\mathrm{d}\ln Q}{\mathrm{d}r}\right|_w + \left(\frac{j\omega}{\lambda_1} - \nu'\right)\left.\frac{\mathrm{d}\ln Q_1}{\mathrm{d}r}\right|_w - \left(\frac{j\omega}{\lambda_2} - \nu'\right)\left.\frac{\mathrm{d}\ln Q_2}{\mathrm{d}r}\right|_w = 0. \tag{14}$$

The implicit relation was used by several authors [Tijdeman, 1975, Stinson, 1991, Bareau and Pagneux,] who used Newton's method to compute m.

2.2.2 Low reduced frequency solution

The model of losses in cylinders initially presented by Zwikker and Kosten [Zwikker and Kosten, 1949] covers almost all applications of musical acoustics. This model is widely used in the musical acoustics community [Chaigne and Kergomard, 2016] even in the case of non-cylindrical tubes [Bilbao and Harrison, 2016, Ernoult and Kergomard, 2020, Tournemenne and Chabassier, 2019]. Stinson [Stinson, 1991] proposed a powerful generalization of this approximation to straight tubes of arbitrary cross-section shape.

The initial derivation by Zwikker and Kosten [Zwikker and Kosten, 1949] made the following assumptions :

- we can assume pressure to be constant on planes orthogonal to the direction of propagation,
- dissipation in the axial direction can be neglected,
- the cross-contribution of viscous and diffusion effects can be neglected.

These assumptions were later shown to be valid by Tijdeman [Tijdeman, 1975] for pipe sizes and frequencies such that :

$$k \ll 1 \quad \text{and} \quad k/s \ll 1, \tag{15}$$

where $k = \omega R/c$ and $s = R\sqrt{\rho_0\omega/\mu}$, are called respectively the reduced frequency and the Stokes number.

The requirement that $k \ll 1$, meaning that the tube is thin compared to the wavelength, is somewhat restrictive. It is verified for the first few harmonics of most instruments, but becomes invalid when considering wide pipes at high frequencies. For example for a pipe of radius $R = 1\,\mathrm{cm}$ and a frequency of $f = 3\,\mathrm{kHz}$, the reduced frequency $k \approx 0.55$ is hardly negligible. Note however that this assumption is pervasive in the acoustics of wind instruments, since it would otherwise be impossible to approximate the three-dimensional wave equation with a one-dimensional "horn equation" [Rienstra, 2005, Chaigne and Kergomard, 2016]. On the other hand, the ratio $k/s = \sqrt{\omega\mu/(\rho_0 c^2)}$ ranges between 1×10^{-4} and 4×10^{-3} at audible frequencies, which validates the second assumption in the context of acoustics.

Under these assumptions, system (3) can be approximated in harmonic regime as:

$$j\omega\hat{\rho}_{ac} + \rho_0 \operatorname{div}\hat{\boldsymbol{v}}_{ac} = 0, \tag{16a}$$

$$\rho_0 j\omega\hat{v}_x = -\partial_x\hat{p}_{ac} + \mu\nabla_T^2\hat{v}_x, \tag{16b}$$

$$\hat{p}_{ac}(x, r) = \hat{p}(x), \tag{16c}$$

$$\rho_0 C_p j\omega\hat{T}_{ac} = \lambda\nabla_T^2\hat{T}_{ac} + j\omega\hat{p}_{ac}, \tag{16d}$$

$$\frac{\hat{p}_{ac}}{p_0} = \frac{\hat{\rho}_{ac}}{\rho_0} + \frac{\hat{T}_{ac}}{T_0}, \tag{16e}$$

where $\nabla_T^2 = \nabla^2 - \dfrac{\mathrm{d}^2}{\mathrm{d}x^2}$ denotes the Laplacian on a cross-section and $\boldsymbol{v}_{ac} = v_x\hat{x} + v_r\hat{r}$.

This system of equations is solved in Appendix B of [Tijdeman, 1975]. Its solution is such that:

$$\frac{\mathrm{d}\hat{p}}{\mathrm{d}x} + \frac{j\omega\rho_0}{1-K_{v0}}\langle\hat{v}_x\rangle = 0 \quad \text{and} \quad \frac{\mathrm{d}\langle\hat{v}_x\rangle}{\mathrm{d}x} + \frac{j\omega}{\rho c^2}(1+(\gamma-1)K_{t0})\hat{p} = 0, \tag{17a}$$

$$K_{v0} = \frac{2J_1(k_vR)}{k_vR\,J_0(k_vR)}, \quad k_v = \sqrt{-\frac{j\omega\rho_0}{\mu}}, \tag{17b}$$

$$K_{t0} = \frac{2J_1(k_tR)}{k_tR\,J_0(k_tR)}, \quad k_t = \sqrt{-\frac{j\omega\rho_0 C_p}{\lambda}}, \tag{17c}$$

$$\langle\hat{v}_x\rangle = \frac{\int_0^R r\hat{v}_x(x,r)dr}{\int_0^R r dr}. \tag{17d}$$

These equations can also be expressed as (ZK) using the total flow across a cross-section $\hat{u} = \pi R^2\langle\hat{v}_x\rangle$.

The moduli of K_{v0} and K_{t0} are displayed in Fig 2 for typical values of radii and frequencies used in musical acoustics, and at a temperature of 20°C. Notice that when the radius and the frequency are small, these coefficients can be larger in modulus than 0.1 (red zone in the figure).

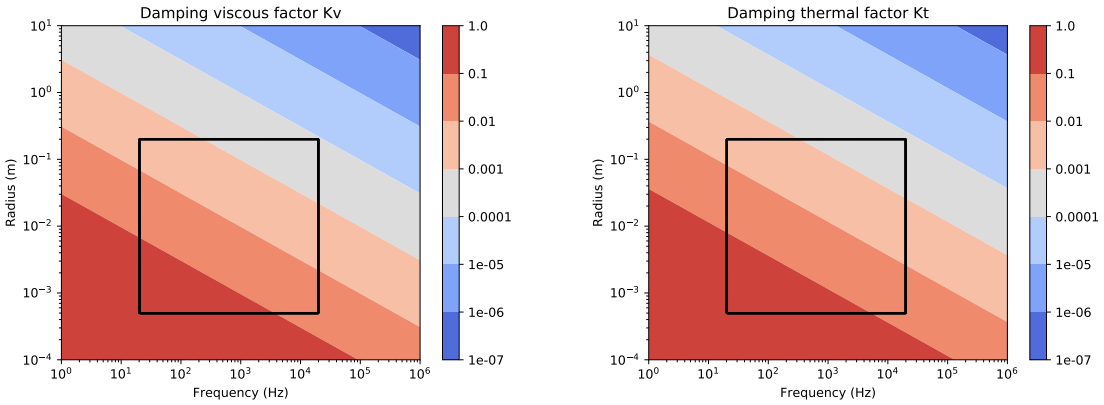

(a) Viscous (b) Thermal

Figure 2: Damping viscous and thermal factors in a cylinder (modulus). The black rectangle represents the range of pipe radii and frequencies of interest in musical acoustics.

2.3 Approximate solutions

Several authors propose methods to approximate the solution to system (3), based on different formulations and numerical techniques.

2.3.1 Particle velocity and temperature variation formulation

In [Joly, 2010] the variables of density and pressure are eliminated while only the acoustic velocity v_{ac} and temperature variation T_{ac} are retained.

$$\begin{cases} \omega^2\boldsymbol{v}_{ac} + B\,\nabla(\nabla\cdot\boldsymbol{v}_{ac}) + C\,\nabla\wedge\nabla\wedge\boldsymbol{v}_{ac} - D\nabla T_{ac} = \mathbf{0} & \text{(18a)} \\ i\omega T_{ac} + Q\,\nabla\cdot(\nabla T_{ac}) - R\nabla\cdot\boldsymbol{v}_{ac} = 0 & \text{(18b)} \end{cases}$$

with

$$B = \frac{c^2}{\gamma} + i\omega c\ell_v, \quad C = -i\omega c\ell'_v, \quad D = i\omega\frac{\hat{\beta}}{\rho_0}, \quad Q = -\gamma\ell_h c, \quad R = \frac{1-\gamma}{\gamma\hat{\beta}}\rho_0 c^2, \tag{19}$$

$$\ell'_v = \frac{\mu}{\rho_0 c}, \quad \ell_h = \frac{\xi}{c}, \quad \ell_v = \frac{\zeta + 4\mu/3}{\rho_0 c} \tag{20}$$

and density and pressure terms can be recovered using formula

$$\rho_{ac} = -\frac{\rho_0}{i\omega}\nabla\cdot\boldsymbol{v}_{ac}, \quad p_{ac} = \hat{\beta}T_{ac} - \frac{\rho_0 c^2}{i\omega\gamma}\nabla\cdot\boldsymbol{v}_{ac} \tag{21}$$

An axisymmetric version of the weak formulation is derived. Then isogeometric elements are considered in the 2D resulting domain. Special care is given to the mesh generation to achieve a numerically significant result, with local refinement close to the boundary layers.

Remark 2. *Note that this technique can present some parametric error-growth phenomena called "locking effect" [Malinen et al., 2004] as k gets small (which is an underlying hypothesis to derive the equations). Using a mixed formulation along with stable finite element discretisation can prevent this issue.*

2.3.2 Mixed formulations

In [Malinen et al., 2004] an auxiliary variable is introduced after scaling of the equations, and is related to the divergence of the acoustic velocity. Then the approximation based on a quadrilateral mesh is an enhancement of the MINI finite element for Stokes equations.

In [Kampinga et al., 2010] another mixed formulation, closer to the original system (3) (only ρ_{ac} is eliminated), is solved using four different types of finite elements : Taylor Hood of different orders, Crouzeix Raviart and MINI. The solved system reads

$$\begin{cases} i\omega\rho_0\boldsymbol{v}_{ac} - ((\zeta+\mu)\nabla(\nabla\cdot\boldsymbol{v}_{ac}) + \mu\Delta\boldsymbol{v}_{ac} - \nabla p_{ac}) = 0 & \text{(22a)} \\ i\omega\rho_0 C_p T_{ac} - \lambda\Delta T_{ac} - i\omega p_{ac} = 0 & \text{(22b)} \\ \nabla\cdot\boldsymbol{v}_{ac} - i\omega\dfrac{T_{ac}}{T_0} + i\omega\dfrac{p_{ac}}{p_0} = 0 & \text{(22c)} \end{cases}$$

2.3.3 Sequential Linearized Navier-Stokes model

In some cases detailed in [Kampinga et al., 2011] (acoustical wave number larger than the viscous and thermal wave numbers, i.e. k/s small), it is justified to neglect the term in blue in Eqs. (22), which characterizes $\boldsymbol{v}_{ac}$ and T_{ac} as solutions to non homogeneous Heat equations where the source term depends on the pressure p_{ac} or its gradient. Therefore it is justified to express the temperature and shear velocity fields with respect to respectively the pressure and its gradient, scaled with scalar potentials that are solution to unitary non homogeneous Heat equations, with pure imaginary squared wavenumber, and with specific boundary conditions (Dirichlet or Neumann depending on the hypotheses on the boundary : no slip / no shear force for the shear velocity and isothermal / adiabatic for the temperature) :

$$\Psi_v + k_v^{-2}\Delta\Psi_v = 1 \quad x\in\Omega \qquad \text{and} \begin{cases} \Psi_v = 0 & \text{(no-slip)} \\ \nabla_n\Psi_v = 0 & \text{(no-shear-force)} \end{cases} \qquad \text{for } x\in\partial\Omega \tag{23}$$

$$\Psi_h + k_h^{-2}\Delta\Psi_h = 1 \quad x\in\Omega \qquad \text{and} \begin{cases} \Psi_h = 0 & \text{(isothermal)} \\ \nabla_n\Psi_h = 0 & \text{(adiabatic)} \end{cases} \qquad \text{for } x\in\partial\Omega \tag{24}$$

where

$$k_v^2 = \frac{-i\omega\rho_0}{\mu}, \quad k_h^2 = \frac{-i\omega\rho_0 C_p}{\lambda} \tag{25}$$

Then the perpendicular component of the acoustical velocity is chosen similar to the shear one and one gets a Helmholtz equation for p_{ac} with non uniform coefficients, that explicitly depend on the pre-computed potentials:

$$\nabla\cdot(\Psi_v\nabla p) + k_0^2\Psi_h' p = 0 \quad \text{for } x\in\Omega \qquad + \text{B.C.} \qquad k_0 = \frac{\omega}{c} \tag{26}$$

where $\Psi_h' = \gamma - (\gamma-1)\Psi_h$. Far from the boundary, the potentials are close to 1 therefore the usual Helmholtz equation is recovered. Close to the boundary, the viscous and thermal effects are accounted for through variation of the coefficients of the equation.

Remark 3. *In the last equation* (26)*, the boundary conditions B.C. can be idealistic or can correspond to an acoustic wall admittance, or even to a coupling with a structure in order to model a viscothermal fluid / structure interaction.*

3 Viscothermal losses as efficient boundary conditions of a homogeneous Helmholtz 3D equation

Since the thermal and viscous effects are preponderant near the boundary, and provided that the boundary layers are small w.r.t. the pipe radius, the pressure field is solution to a homogeneous Helmholtz equation on most of the domain (far from the boundaries), while its behaviour is more complex near the boundaries. It is thus tempting to model the phenomenon as artificial boundary conditions of the "interior" domain where a usual Helmholtz equation is posed, these conditions being inferred from experiments or from mathematical methods. This is the object of this section, which explores two possible boundary conditions that mimic the presence of viscous and thermal boundary layers. Notice that in this case, the considered domain is smaller that the actual pipe, and the pressure field is not computed where viscous and thermal effects are large.

Let us consider the 3D acoustic equations in the acoustic region of the pipe (excluding the viscothermal boundary layers), solved by the pressure $\hat{p}_{ac}$ and the acoustical velocity $\hat{v}_{ac}$ such that

$$\begin{cases} \nabla \hat{p}_{ac}(x) + j\omega\rho \hat{v}_{ac}(x) = 0 \Rightarrow v_{ac}\cdot n = -\dfrac{\nabla p_{ac}\cdot n}{j\omega\rho} & \text{(27a)} \\ \operatorname{div} \hat{v}_{ac}(x) + j\omega \dfrac{1}{\rho c^2}\hat{p}_{ac}(x) = 0 & \text{(27b)} \end{cases}$$

The input impedance of the pipe defined from the averaged variables mean flow u and mean pressure p such that $p = \displaystyle\int_{\Gamma_{\text{in}}} p_{ac}$ and $u/S = \displaystyle\int_{\Gamma_{\text{in}}} v_{ac}$ can be written according to the acoustic 3D variables as

$$Z_{\text{in}} = \frac{p}{u} = \frac{\int_{\Gamma_{\text{in}}} \hat{p}_{ac}}{S\int_{\Gamma_{\text{in}}} \hat{v}_{ac}\cdot n} = \frac{\int_{\Gamma_{\text{in}}} \hat{p}_{ac}}{\int_{\Gamma_{\text{in}}} \nabla \hat{p}_{ac}\cdot n}\frac{i\omega\rho}{S} = -\frac{\int_{\Gamma_{\text{in}}} \hat{p}_{ac}}{\int_{\Gamma_{\text{in}}} \partial_z \hat{p}_{ac}}\frac{i\omega\rho}{S} \tag{28}$$

Remark 4. *Notice that the definition of the input impedance given in Eq. 28 is based on the pressure and flow averaged on the interior domain, excluding what happens in the viscothermal boundary layers. In Sec. 5 we will compare input impedances computed from different models that do not have the same definition. More precisely, for the 1D models derived in Sec. 4, the definition of the 1D variable associated with the flow is not always the same. For the Zwikker and Kosten model* (ZK)*, the average is taken on all the section (including the viscothermal boundary layers) whereas for the Webster-Lokshin model* (53)*, the average is done on the interior domain which excludes the bounday layers.*

3.1 Cremer boundary conditions

In [Cremer, 1948] is derived the wall admittance for a plane wave hitting an infinite plane wall of normal e_x

$$\frac{\hat{v}_{ac}\cdot n}{\hat{p}_{ac}} = Y_w = \frac{1}{\rho c}\sqrt{\frac{j\omega}{c}}\left[\left(1-\frac{k_x^2}{k^2}\right)\sqrt{\ell_v} + (\gamma-1)\sqrt{\ell_t}\right]\left(= \frac{-\nabla \hat{p}_{ac}\cdot n}{j\omega\rho\,\hat{p}_{ac}}\right) \tag{29}$$

where

$$\ell_v = \frac{\mu}{\rho c} \quad \text{and} \quad \ell_t = \frac{\lambda}{\rho c C_p}.$$

The factor $1-\dfrac{k_x^2}{k^2}$ quantifies the direction of the plane wave with respect to the wall. Extending this condition to a plane wave in a cylinder leads to $k_x = 0$. It is cited in [Bruneau et al., 1989] to derive dispersion relations. In [Bossart et al., 2003] equivalent boundary conditions (Eq. 15b, 15d) for closing Helmholtz equation are derived from the analysis and computation of boundary layers coming from thermo-viscous equations:

$$(\partial_u - ik_0\beta)p_{ac} = 0, \text{ where } \beta = k_0\left(\frac{k_w^2}{k_0^2 k_v} + \frac{\gamma-1}{k_h}\right), \quad k_0 = \frac{\omega}{c}, \quad k_v = (1-i)\sqrt{\frac{k_0}{2\ell_v}}, \quad k_h = (1-i)\sqrt{\frac{k_0}{2\ell_t}} \tag{30}$$

A predictor-corrector approach is followed to estimate $\dfrac{k_w^2}{k_0^2}$: a first simulation is run by setting its value to 1/2, leading to an estimated value which is used to run a second simulation. In [Lefebvre and Scavone, 2010] FEM are used on a Helmholtz equation in the domain, closed with equivalent boundary conditions (Eq. 1 of the paper)

$$Y_w = \frac{1}{\rho c}\sqrt{\frac{j\omega}{c}}\left[\sin^2\theta\sqrt{\ell_v} + (\gamma-1)\sqrt{\ell_t}\right] \tag{31}$$

where θ is said to be the angle of incidence of the wave. In [Lefebvre et al., 2013] the same wall admittance is used to closed a Helmholtz equation, and an iterative procedure is followed to estimate θ "until convergence is found".

Remark 5. *Note that for a plane wave in a cylinder with Neumann BC, we would have $k_x = 0$, i.e. $\theta = \pi/2$, and the condition would write*

$$Y_w = \frac{1}{\rho c}\sqrt{\frac{j\omega}{c}}\left[\sqrt{\ell_v} + (\gamma - 1)\sqrt{\ell_t}\right] \tag{32}$$

This condition is the starting point for Webster-Lokshin 1D models used in [Hélie et al., 2013], further discussed in Sec. 4.4.

3.2 Viscothermal boundary conditions

More recently, [Jith and Sarkar, 2018] and [Berggren et al., 2018] proposed to model the angle of incidence using a Laplace-Beltrami operator at the boundary :

$$-\delta_v \frac{i-1}{2}\Delta_T \hat{p}_{ac} + \delta_T k_0^2 \frac{(i-1)(\gamma-1)}{2}\hat{p}_{ac} + \frac{\partial \hat{p}_{ac}}{\partial n} = 0 \tag{33}$$

They both amount to the same following condition

$$\sqrt{\frac{-i\mu}{\rho\omega}}\Delta_T \hat{p}_{ac} - \left(\frac{\omega}{c}\right)^2 (\gamma - 1)\sqrt{\frac{-i\lambda}{\omega\rho C_p}}\hat{p}_{ac} + \frac{\partial \hat{p}_{ac}}{\partial n} = 0 \tag{34}$$

where p_{ac} is the acoustical pressure, solution to

$$-\Delta \hat{p}_{ac}(x) - \left(\frac{\omega}{c}\right)^2 \hat{p}_{ac}(x) = 0 \tag{35}$$

which is derived by eliminating the acoustical velocity $\hat{v}_{ac}$ in Eq. (27).

Remark 6. *When the pipe is a cylinder and we consider the lossless propagation of the first transversal mode which is planar, then the pressure is constant in the radial direction of the pipe, meaning that the term $\Delta_T \hat{p}_{ac}$ is equal to $\Delta \hat{p}_{ac}$. From the volumic equation we get that this term is in fact equal to $-\omega^2 \hat{p}_{ac}/c^2$ and we recover Cremer condition Eq. (29) with $k_x = 0$ leading to the wall admittance (32). This is only an approximation as soon as the boundary conditions are not perfect.*

Remark 7. *In [Berggren et al., 2018] an asymptotic approach is followed, that separates the effect of the viscous and thermal boundary layers close to the wall, and of the acoustic wave propagation in the rest of the domain. This approach is valid as soon as the boundary layers are small with respect to the radius, i.e. $s \gg 1$. The variables are then scaled closed to the wall and a new system is derived (similar to Eqs. (16) but only valid in the boundary layers), after having supposed that $\epsilon = (k/s)^2 \ll 1$, that has an analytic solution.*

3.3 Finite Elements Implementation

The aim of this section is to run simulations on a 3D axisymmetric domain following the linear acoustic equations, where the boundary conditions on the walls of the pipe are those seen above. They will be used in Sec. 5 to compare with several 1D models. We use the opensource finite elements library Montjoie (montjoie.gforge.inria.fr) to perform the simulations. In Montjoie the following generic equation is solved in an axisymmetric setting:

$$\begin{cases} \left(-\rho_M \omega^2 - i\omega\sigma_M\right) u_M - \operatorname{div}\left(\mu_M \nabla u_M\right) = f_M & \text{for } x \in \Omega \\ \mu\left(c_M \dfrac{\partial u_M}{\partial n} + Z_M u_M + \delta_M \Delta_T u_M\right) = g_M & \text{for } x \in \partial\Omega \end{cases} \tag{36}$$

For dealing with problem (34-35) we set

$$u_M = p_{ac}, \quad \rho_M = \frac{1}{c^2}, \quad \mu_M = 1, \quad \sigma_M = 0, \quad f_M = 0, \quad \begin{cases} g_M = 0 \text{ on } \Gamma_{\text{wall}}, \\ c_M = 0,\ Z_M = 1,\ \delta_M = 0 \text{ and } g_M = 0 \text{ on } \Gamma^+, \\ Z_M = 0,\ \delta_M = 0 \text{ and } g_M = G(r) \text{ on } \Gamma^-. \end{cases}$$

An adaptation part is added at the bottom edge of the geometry of interest in order to apply a boundary source which is compatible with the tested boundary conditions, see Fig. 3. The source of the problem is chosen

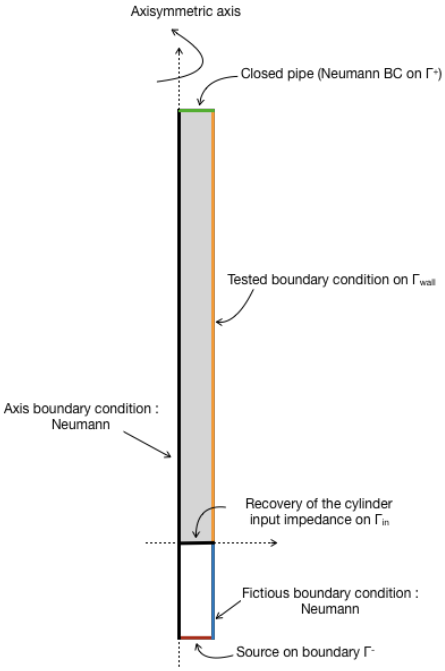

Figure 3: Geometry used for Montjoie axisymmetric computation of a cylinder input impedance. The cylinder of interest is highlighted in grey. The white part is an adaptation cylinder with non dissipative boundary conditions.

as a Dirichlet boundary condition on the entry Γ^- (source on the pressure). The pipe is considered to be closed at the top on Γ^+, leading to a Neumann boundary condition (null acoustic velocity). The function $G(r)$ is set to a constant value (the source is a constant pressure on the entry surface). Regarding the coefficients on the wall Γ_{wall}, we have implemented two boundary conditions.

- **Cremer boundary conditions** The coefficients for Γ_{wall} are set to

$$Z_M = -\left(\frac{\omega}{c}\right)^2 \left[\sqrt{\frac{-i\mu}{\rho\omega}} + (\gamma-1)\sqrt{\frac{-i\kappa}{\omega\rho C_p}}\right], \qquad \delta_p = 0, \qquad c_M = 1 \tag{37}$$

  Therefore, $Z_M = Y_p i\omega\rho$ where Y_p coincides with Y_w defined as (32), and $\delta_p = 0$, which will be called "Cremer BC" in the sequel.

- **Viscothermal boundary layer conditions** To fit the boundary condition (34), which will be called "Visco BC", the coefficients for Γ_{wall} are set to

$$Z_M = -\left(\frac{\omega}{c}\right)^2 (\gamma-1)\sqrt{\frac{-i\kappa}{\omega\rho C_p}}, \qquad \delta_p = \sqrt{\frac{-i\mu}{\rho\omega}}, \qquad c_M = 1 \tag{38}$$

3.3.1 Cylindrical case

In a 20 cm long cylinder of radius 4 mm, we solve the previous system for $f = 1$ kHz and a temperature of 20 Celsius degrees. The mesh is composed of quadrangles with a characteristic length of 4 mm. The test case is done with a Dirichlet surfacic source G begin constant on Γ^-. The solution's convergence is not easy to reach because of evanescent modes close to the pipe entry Γ_{in} (where the exterior boundary condition changes). Refining the mesh close to this point allows to achieve the convergence curves displayed in Fig 4 on the input impedance, for both tested boundary conditions. The pressure, its longitudinal derivative and therefore the impedance computed using formula Eq. (28) on Γ_{in} converge as the order increases.

In Fig. 5 is displayed the real part of the pressure in the on the half plane $y = 0 \times x \geq 0$. There is no visual difference between the two solutions. Their relative L^2 difference on the half plane is equal to 0.625 %. The pressure and its derivatives are displayed in Fig. 6 for both BCs. Finaly, if we compute the input impedance of the cylinder with both methods, their relative error is of 2.104 %.

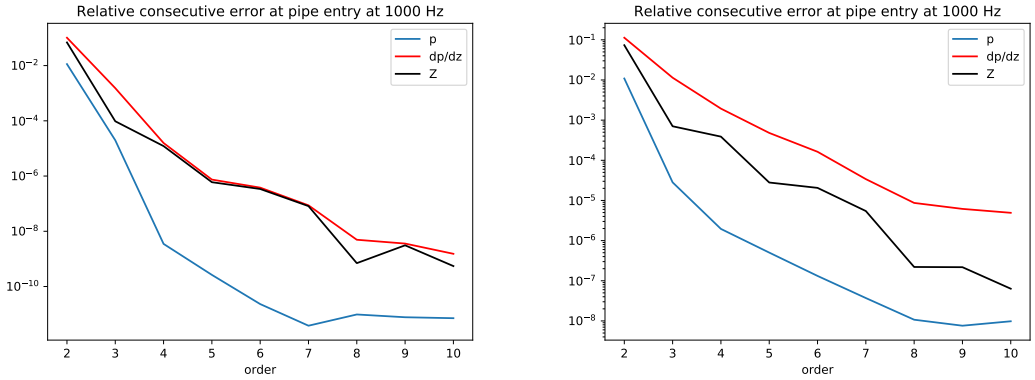

(a) Cremer (b) Visco

Figure 4: Consecutive relative L2 error on the half plane $z = 0$ w. r. t. FEM order.

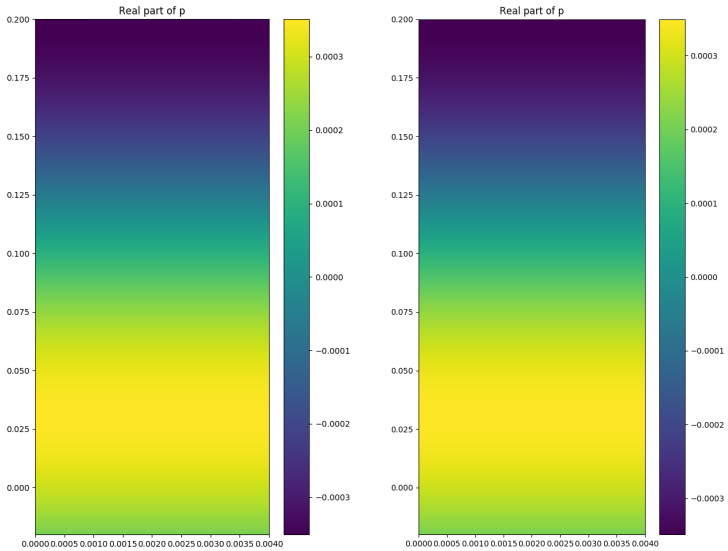

Figure 5: Real part of the pressure on the half plane $y = 0 \times x \geq 0$, obtained with Cremer (left) and Visco (right) BC.

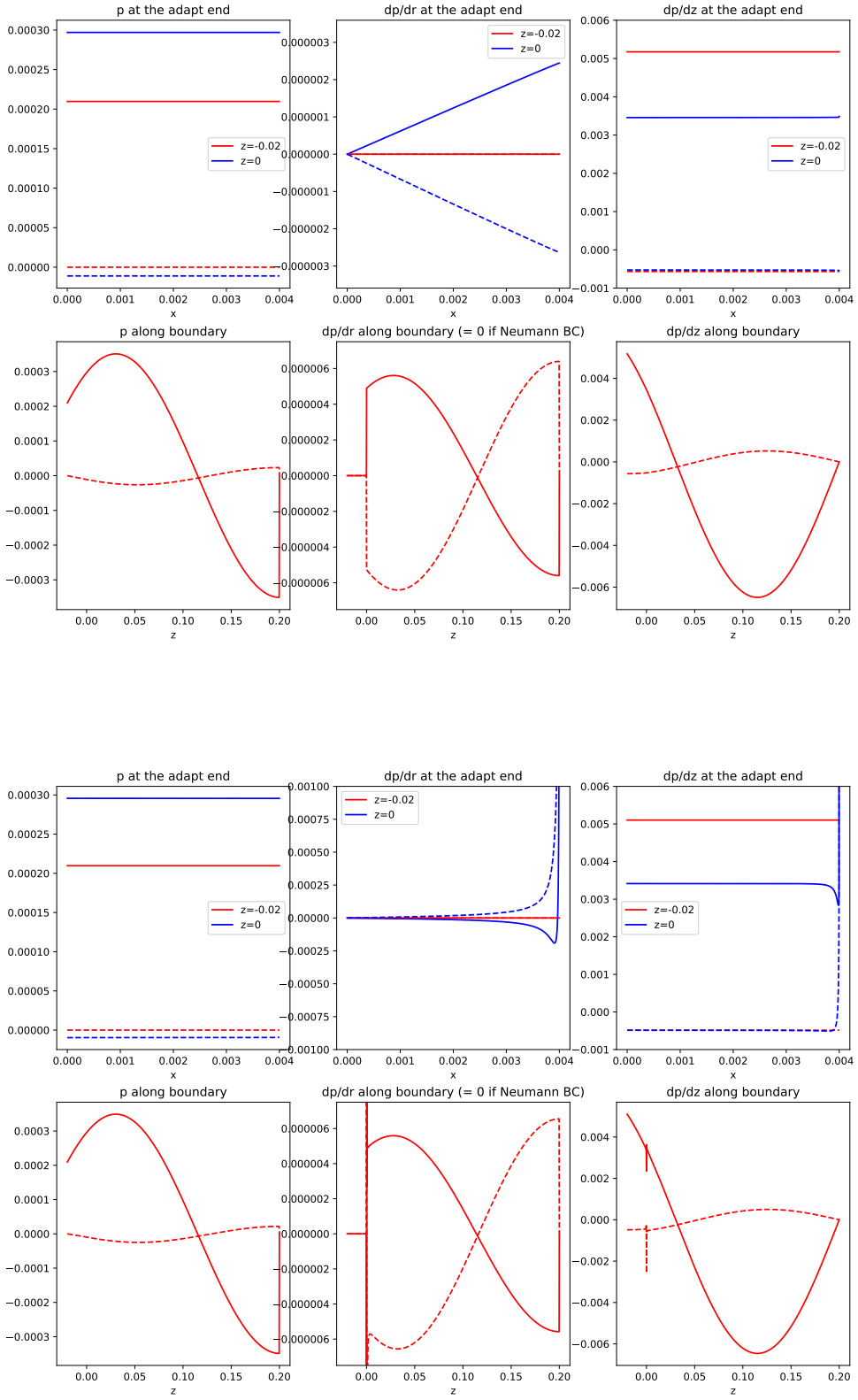

Figure 6: Pressure and its derivatives along Γ^- ($z = -0.02$), Γ_{in} ($z = 0$) and Γ_{wall} (along z), obtained with Cremer (top) and Visco (bottom) BC.

3.3.2 Conical case

In order to test the boundary conditions in a conical geometry, in conditions comparable to input impedance measurements, the question of source surfacic boundary condition arises. Indeed, spherical waves can establish in a conical geometry, provided that the boundary conditions are compatible with this type of waves, i.e. that the boundary conditions are set on a spherical cap at the entry and end of the pipe. On the contrary, if the boundary conditions are set on plane surfaces, this will constraint the waves inside the pipe and force planar waves. For this reason, we will be able to test two hypotheses for the computation of the input impedance in the cone : "planar waves" and "spherical waves".

Moreover, for the same reasons as in the cylindrical case (compatibility of source surfacic boundary conditions and tested boundary condtions), we add an adaptation part before the actual tested cone. We have tried to make this part either a cylinder or a cone with the same angle as the tested cone, as illustrated in Fig. 7.

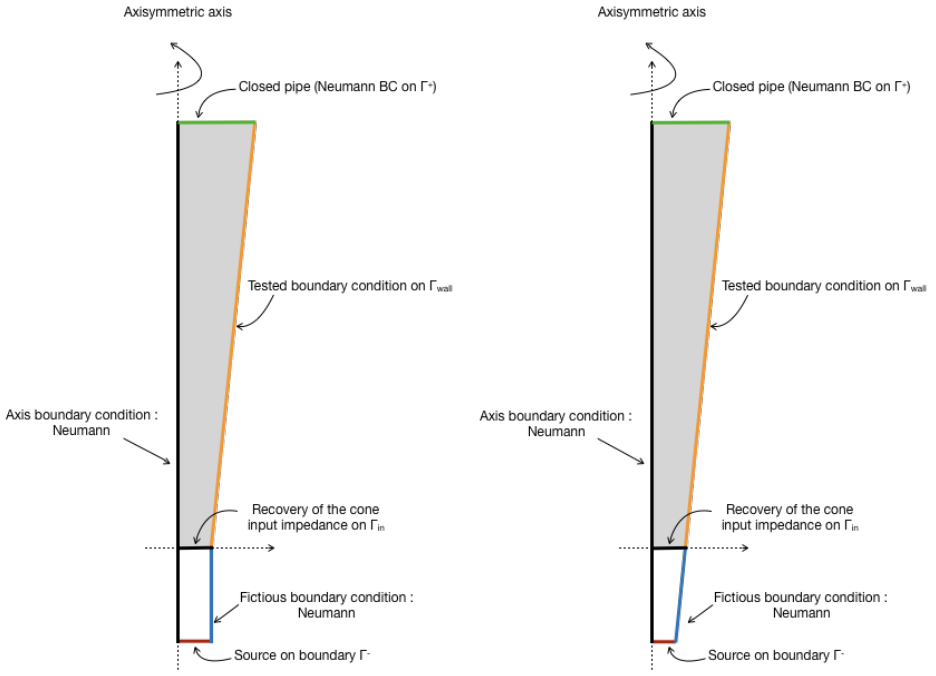

(a) Cylindrical adaptation part (b) Conical adaptation part

Figure 7: Geometry used for Montjoie axisymmetric computation of a cone input impedance. The cone of interest is highlighted in grey. The white part is an adaptation cylinder or cone with non dissipative boundary conditions.

Consequently, four configurations arise :

1. Cylindrical adaptation part with planar surfaces Γ^- and Γ^+
2. Cylindrical adaptation part with planar surface Γ^- and spherical surface Γ^+
3. Conical adaptation part with planar surfaces Γ^- and Γ^+
4. Conical adaptation part with spherical surfaces Γ^- and Γ^+

However, in all the configurations, the input impedance is computed on the surfacic plane Γ_{in}. This could be improved in future work by considering pressure and acoustic velocity on the cone entry spherical cap.

We consider a 20 cm long cone with entry radius of 4 mm and ending radius of 8 mm. We solve the previous system for $f = 2$ kHz and a temperature of 20 Celsius degrees. The mesh is composed of quadrangles with a characteristic length of 2 mm. A refinement of the mesh is done at the global scale towards the planar surface Γ_{in} and at the local scale close to the end points of the boundary Γ_{wall} and the axis point of the boundary Γ^+. The test case is done with a Dirichlet surfacic source G being constant on Γ^-. The convergence curves for configuration 4 are displayed for both tested boundary conditions in Fig 8

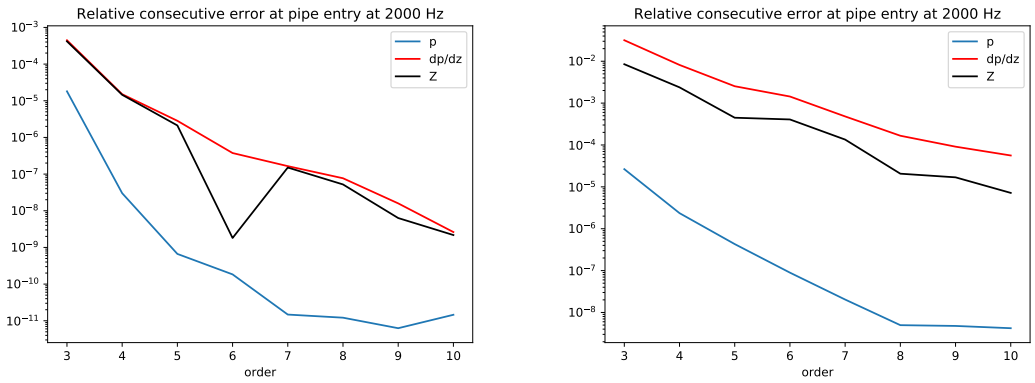

(a) Cremer (b) Visco

Figure 8: Consecutive relative L2 error on the half plane $z = 0$ w. r. t. FEM order.

4 Viscothermal 1D models

In this section we explore several 1D reduced models which are used in musical acoustics in cases where the linear regime is valid. Let us introduce the non dimension viscous and thermal reduced frequencies (notice that the viscous reduced frequency is also what is called s, the Stokes number, in this report)

$$r_v = R\sqrt{\frac{\omega\rho}{\mu}} \equiv s \quad \text{and} \quad r_t = R\sqrt{\frac{\omega\rho C_p}{\kappa}}$$

4.1 Lossless case

When assuming planar waves (valid for example in a cylinder) and neglecting losses, acoustic waves are solution to:

$$\begin{cases} \dfrac{d\hat{p}}{dx} + j\omega\dfrac{\rho}{S}\hat{u} = 0, & \text{(39a)} \\ \dfrac{d\hat{u}}{dx} + j\omega\dfrac{S}{\rho c^2}\hat{p} = 0, & \text{(39b)} \end{cases}$$

where $\hat{p}$ is the complex amplitude of the acoustic pressure on the plane of abscissa x, and $\hat{u}$ is the complex amplitude of the acoustic flow crossing that plane toward positive x. This equation is also derived in [Rienstra, 2005] from a asymptotic analysis in an axisymmetric domain where the acoustical wavelength is large with respect to the domain radius.

4.2 Zwikker and Kosten formulation

In [Zwikker and Kosten, 1949] and later shown in [Tijdeman, 1975] by following the approach recalled in Sec. 2.2.2, the following model is a good approximation for the average fields of thermoviscous waves in a cylinder :

$$\begin{cases} \dfrac{d\hat{p}}{dx} + j\omega\dfrac{\rho}{S}\hat{u} + j\omega\dfrac{\rho}{S}\dfrac{\mathcal{J}(\sqrt{-j}r_v)}{1-\mathcal{J}(\sqrt{-j}r_v)}\hat{u} = 0, \\ \dfrac{d\hat{u}}{dx} + j\omega\dfrac{S}{\rho c^2}\hat{p} + j\omega\dfrac{S}{\rho c^2}(\gamma-1)\mathcal{J}(\sqrt{-j}r_t)\hat{p} = 0. \end{cases} \quad \text{(ZK)}$$

with

$$\mathcal{J}(\alpha) = \frac{2J_1(\alpha)}{\alpha J_0(\alpha)}, \quad \forall\alpha \in \mathbb{C} \tag{40}$$

where J_0 and J_1 are zeroth- and first-order Bessel functions.

4.3 Keefe formulation for wide pipes and high frequency (large s)

4.3.1 Original model

This approximation derived for large values of s in [Keefe, 1984] (see Fig. 9) stands that

$$\mathcal{J}(\sqrt{-j}x) \approx \frac{2\sqrt{-j}}{x} + \frac{j}{x^2} \quad \text{(Approx-Keefe)}$$

where we define that

$$\sqrt{-j} = \frac{1-j}{\sqrt{2}} \tag{41}$$

The approximate model reads

$$\begin{cases} \dfrac{d\hat{p}}{dx} + j\omega\dfrac{\rho}{S}\hat{u} + j\omega\dfrac{\rho}{S}\left[\dfrac{2\sqrt{-j}}{r_v} - \dfrac{3j}{r_v^2}\right]\hat{u} = 0, & \text{(42a)} \\ \dfrac{d\hat{u}}{dx} + j\omega\dfrac{S}{\rho c^2}\hat{p} + j\omega\dfrac{S}{\rho c^2}(\gamma-1)\left[\dfrac{2\sqrt{-j}}{r_t} + \dfrac{j}{r_t^2}\right]\hat{p} = 0. & \text{(42b)} \end{cases}$$

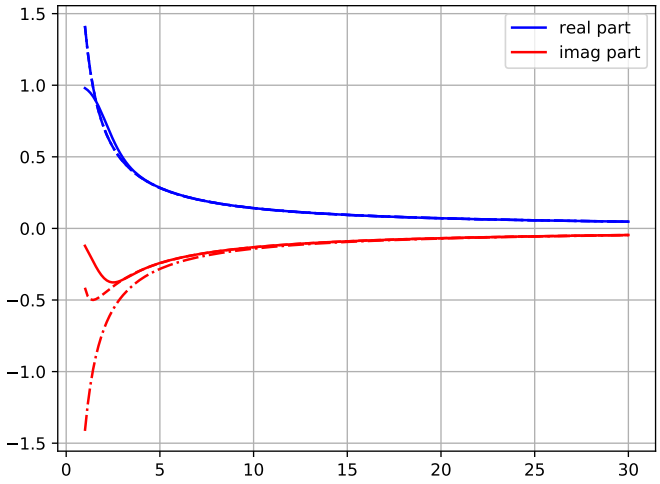

Figure 9: Real and imaginary parts of $\mathcal{J}(\sqrt{-j}x)$ (solid lines), its approximation (Approx-Keefe) (dashed lines) and its approximation (Approx-truncated-Keefe) (dotted lines) for $x \in [1, 30]$.

This gives

$$\begin{cases} \dfrac{d\hat{p}}{dx} + j\omega\dfrac{\rho}{S}\hat{u} + j\omega\dfrac{\rho}{S}\left[\dfrac{2}{R}\sqrt{\dfrac{-j\mu}{\omega\rho}} - \dfrac{3}{R^2}\dfrac{j\mu}{\omega\rho}\right]\hat{u} = 0, & \text{(43a)} \\ \dfrac{d\hat{u}}{dx} + j\omega\dfrac{S}{\rho c^2}\hat{p} + j\omega\dfrac{S}{\rho c^2}(\gamma-1)\left[\dfrac{2}{R}\sqrt{\dfrac{-j\kappa}{\omega\rho C_p}} + \dfrac{1}{R^2}\dfrac{j\kappa}{\omega\rho Cp}\right]\hat{p} = 0. & \text{(43b)} \end{cases}$$

4.3.2 Simplified model

A less accurate approximation (see Fig. 9) is given by

$$\mathcal{J}(\sqrt{-j}x) \approx \frac{2\sqrt{-j}}{x} \qquad \text{(Approx-truncated-Keefe)}$$

This yields

$$\begin{cases} \dfrac{d\hat{p}}{dx} + j\omega\dfrac{\rho}{S}\hat{u} + j\omega\dfrac{\rho}{S}\dfrac{2}{R}\sqrt{\dfrac{-j\mu}{\omega\rho}}\hat{u} = 0, & \text{(44a)} \\ \dfrac{d\hat{u}}{dx} + j\omega\dfrac{S}{\rho c^2}\hat{p} + j\omega\dfrac{S}{\rho c^2}(\gamma-1)\dfrac{2}{R}\sqrt{\dfrac{-j\kappa}{\omega\rho C_p}}\hat{p} = 0. & \text{(44b)} \end{cases}$$

In the case of a cylinder (R is constant), $\hat{p}$ solves the following equation

$$-\frac{d^2\hat{p}}{dx^2} - \frac{\omega^2}{c^2}\hat{p} - \frac{\omega^{3/2}}{c^2}\frac{2}{R}\left[\sqrt{\frac{-j\mu}{\rho}} + (\gamma-1)\sqrt{\frac{-j\kappa}{\rho C_p}}\right]\hat{p} - \frac{\omega}{c^3}\frac{4}{R^2}\sqrt{\frac{-\mu\kappa}{\rho C_p}}\hat{p} = 0 \qquad (45)$$

while $\hat{u}$ can be recovered by

$$\hat{u} = -\frac{1}{j\omega}\frac{S}{\rho}\frac{1}{1 + j\omega\dfrac{\rho}{S}\dfrac{2}{R}\sqrt{\dfrac{-j\mu}{\omega\rho}}}\frac{d\hat{p}}{dx} \qquad (46)$$

4.3.3 Half-approximated model

In [Bilbao and Chick, 2013] is used a model lying between the two previous approximations. Terms in $1/r_t^2$ are dropped but terms in $1/r_v$ are kept, for causality reasons. It reads

$$\begin{cases} \dfrac{d\hat{p}}{dx} + j\omega\dfrac{\rho}{S}\hat{u} + j\omega\dfrac{\rho}{S}\left[\dfrac{2\sqrt{-j}}{r_v} - \dfrac{3j}{r_v^2}\right]\hat{u} = 0, & \text{(47a)} \\ \dfrac{d\hat{u}}{dx} + j\omega\dfrac{S}{\rho c^2}\hat{p} + j\omega\dfrac{S}{\rho c^2}(\gamma-1)\dfrac{2\sqrt{-j}}{r_t}\hat{p} = 0. & \text{(47b)} \end{cases}$$

This gives

$$\begin{cases} \dfrac{d\hat{p}}{dx} + j\omega\dfrac{\rho}{S}\hat{u} + j\omega\dfrac{\rho}{S}\left[\dfrac{2}{R}\sqrt{\dfrac{-j\mu}{\omega\rho}} - \dfrac{3}{R^2}\dfrac{j\mu}{\omega\rho}\right]\hat{u} = 0, & \text{(48a)} \\ \dfrac{d\hat{u}}{dx} + j\omega\dfrac{S}{\rho c^2}\hat{p} + j\omega\dfrac{S}{\rho c^2}(\gamma-1)\dfrac{2}{R}\sqrt{\dfrac{-j\kappa}{\omega\rho C_p}}\hat{p} = 0. & \text{(48b)} \end{cases}$$

4.4 Expressing the Webster–Lokshin model as a Telegraphist's Equation

The Webster–Lokshin model as described in [Hélie et al., 2013], is expressed in the harmonic domain as:

$$\left(\partial_\ell^2 + 2\frac{\mathcal{R}'(\ell)}{\mathcal{R}(\ell)}\partial_\ell - \frac{1}{c^2}(j\omega)^2 - \frac{2\varepsilon(\ell)}{c^{3/2}}(j\omega)^{3/2}\right)\hat{p}(\ell,t) = 0, \tag{49}$$

$$j\omega\rho\hat{v}(\ell,t) + \partial_\ell p(\ell,t) = 0, \tag{50}$$

where

- The unknown $\hat{p}(\ell,t)$ is the complex amplitude of the acoustic pressure along the curvilinear abscissa ℓ following the bore profile.
- The unknown $\hat{v}$ is the longitudinal air velocity away from the boundary layers.
- The function $\mathcal{R}(\ell)$ is the radius of the bore as a function of the curvilinear abscissa. It corresponds to a change of variables of the function $R(z)$ which describes the bore radius as a function of axial abscissa: $\mathcal{R}(\ell) = R(L^{-1}(\ell))$, where
$$L(x) = \int_0^x \sqrt{1 + R'(s)^2}ds.$$
- Function $\varepsilon(\ell) = \varepsilon^* \dfrac{\sqrt{1-\mathcal{R}'(\ell)^2}}{\mathcal{R}(\ell)}$, where
$$\varepsilon^* = \sqrt{l_v} + (\gamma-1)\sqrt{l_t} \approx 3.125 \times 10^{-4}\,\mathrm{m}^{1/2},$$
comes from Cremer's boundary conditions described in Sec. 3.1 and can be rewritten as a function of z,
$$\varepsilon(L(z)) = \frac{\varepsilon^*}{R(z)\sqrt{1+R'(z)^2}}.$$
- ω is the angular frequency, c is the speed of sound, j is the imaginary unit.

To be used in OpenWIND, the model must be expressed as a telegraphist's equation of the form:

$$\begin{cases} Z_v\hat{u} + \partial_x\hat{p} = 0, \\ Y_t\hat{p} + \partial_x\hat{u} = 0. \end{cases} \tag{51}$$

Denoting $S(x) = \pi R(x)^2$ the section of the tube, it is possible to set $\hat{u} = S\hat{v}$ and obtain:

$$\begin{cases} Z_v(x) = j\omega\dfrac{\rho}{S(x)}L'(x), \\ Y_t(x) = j\omega\dfrac{S(x)}{\rho c^2}L'(x)(1+\mathcal{Y}(x)), \\ \mathcal{Y}(x) = 2\varepsilon(L(x))\left(\dfrac{j\omega}{c}\right)^{-1/2}. \end{cases} \tag{52}$$

Noting that $\dfrac{d}{d\ell} = \dfrac{1}{L'(x)}\dfrac{d}{dx}$, we see that eliminating $\hat{u}$ and replacing coefficients Z_v and Y_t into (51) yields (49).

The corresponding system in the common form is:

$$\begin{cases} \dfrac{\mathrm{d}\hat{p}}{\mathrm{d}x} + j\omega\dfrac{\rho}{S}\sqrt{1+R'^2}\,\hat{u} = 0, & \text{(53a)} \\ \dfrac{\mathrm{d}\hat{u}}{\mathrm{d}x} + j\omega\dfrac{S}{\rho c^2}\sqrt{1+R'^2}\,\hat{p} + j\omega\dfrac{S}{\rho c^2}\dfrac{2}{R}\left[\sqrt{\dfrac{-j\mu}{\omega\rho}} + (\gamma-1)\sqrt{\dfrac{-j\kappa}{\omega\rho C_p}}\right]\hat{p} = 0. & \text{(53b)} \end{cases}$$

4.4.1 Case of the cylinder

In this case, $R' = 0$. System (53) reduces to

$$\begin{cases} \dfrac{d\hat{p}}{dx} + j\omega \dfrac{\rho}{S}\, \hat{u} = 0, & \text{(54a)} \\ \dfrac{d\hat{u}}{dx} + j\omega \dfrac{S}{\rho c^2}\hat{p} + j\omega \dfrac{S}{\rho c^2}\dfrac{2}{R}\left[\sqrt{\dfrac{-j\mu}{\omega\rho}} + (\gamma-1)\sqrt{\dfrac{-j\kappa}{\omega\rho C_p}}\right]\hat{p} = 0. & \text{(54b)} \end{cases}$$

Eliminating $\hat{u}$ yields the following second order equation on $\hat{p}$:

$$-\frac{d^2\hat{p}}{dx^2} - \frac{\omega^2}{c^2}\hat{p} - \frac{\omega^{3/2}}{c^2}\frac{2}{R}\left[\sqrt{\frac{-j\mu}{\rho}} + (\gamma-1)\sqrt{\frac{-j\kappa}{\rho C_p}}\right]\hat{p} = 0 \tag{55}$$

In this equation, the term $-\dfrac{\omega}{c^3}\dfrac{4}{R^2}\sqrt{\dfrac{-\mu\kappa}{\rho C_p}}\hat{p}$ is missing to recover Eq. (45), which is an approximated version of system (43), which itself approaches system (ZK).

4.4.2 On the definition of the flow

It is interesting to note that in system (53), the unknown $\hat{u}$ does not have the same meaning as in system (44). Indeed, when writing $\hat{u} = S\hat{v}$, we neglect the influence of boundary layers on the expression of flow. To take this effect into account, $\hat{u}$ should contain a correction factor to account for the presence of boundary layers:

$$\hat{u}_{corr} = (1 - K_v)\, S\hat{v}, \tag{56}$$

where K_v is given by $\mathcal{J}(\sqrt{-j}r_v) = \dfrac{2J_1(k_vR)}{k_vR\,J_0(k_vR)}$ (17b), or an approximation thereof as (Approx-Keefe) of (Approx-truncated-Keefe).

This has an impact on the definition of the input impedance: if we denote by $Z_{WL} = \hat{p}/\hat{u}$ the impedance given by the Webster–Lokshin model, and $Z_{corr} = \hat{p}/\hat{u}_{corr}$ the impedance with the correcting factor, one has:

$$Z_{corr}(\ell,\omega) = \frac{1}{1 - K_v(\ell,\omega)} Z_{WL}(\ell,\omega). \tag{57}$$

This correcting factor is more important for thinner pipes, and at lower frequencies (see Fig. 2(a)). It must be applied when estimating the input impedance, but also when expressing the radiation impedance at the instrument bell.

4.5 Towards time domain formulations of 1D-models

4.5.1 Diffusive representations of Zwikker and Kosten (ZK) system.

In [Thompson et al., 2014] continued fractions are used to approximate the coefficients of Eq. (ZK). In [Bilbao et al., 2015], [Bilbao and Harrison, 2016] a diffusive representation with Foster structure is used to approximate the coefficients of Eq. (ZK). This leads to a system of the following form, obtained by direct manipulations of Eq. (12-16) of [Bilbao and Harrison, 2016],

$$\begin{cases} \dfrac{j\omega\,\rho}{S}\hat{u} + \dfrac{d\hat{p}}{dx} + \dfrac{R_0}{S}\hat{u} + \displaystyle\sum_{i=1}^{M}\frac{R_i}{S}(\hat{u} - \hat{u}_i) = 0 \\ \dfrac{j\omega\,S}{\rho c^2}\hat{p} + \dfrac{d\hat{u}}{dx} + SG_0(p - p_0) + \displaystyle\sum_{i=1}^{M} SG_i(\hat{p} - \hat{p}_0 - \hat{p}_i) = 0 \\ j\omega\, L_i\hat{u}_i = R_i(\hat{u} - \hat{u}_i) \qquad \forall\, 1 \le i \le M \\ j\omega\, C_0\hat{p}_0 = G_0(\hat{p} - \hat{p}_0) + \displaystyle\sum_{i=1}^{M} G_i(\hat{p} - \hat{p}_0 - \hat{p}_i) \\ j\omega\; C_i\hat{p}_i = G_i(\hat{p} - \hat{p}_0 - \hat{p}_i) \qquad \forall\, 1 \le i \le M \end{cases}$$

In this model, $2M+1$ additional variables homogeneous to acoustic pressure $\hat{p}_0$, $\hat{p}_i$ and to acoustic flow $\hat{u}_i$ for $1 \le i \le M$ are introduced and the coefficients C_i, G_i, L_i, R_i are computed following [Bilbao and Harrison, 2016] using an optimisation routine for each radius value. Note that this method is also used in [Schmutzhard et al., 2017].

4.5.2 Diffusive representation of Webster-Lokshin (53) equation.

In [Hélie and Matignon, 2006] a diffusive representation of the transfer functions associated with Webster-Lokshin (53) equation is proposed. This leads to the introduction of a series of auxiliary variables ϕ_i and ϕ'_k such that

$$\begin{cases} j\omega\phi_i = -\xi_i\phi_i + u \quad 1 \leq i \leq J & \text{(58a)} \\ j\omega\phi'_k = (-\xi'_k + j\omega'_k)\phi'_k + u \quad 1 \leq k \leq K & \text{(58b)} \\ y = \displaystyle\sum_{i=1}^{J} \mu_j\phi_j + 2\Re\sum_{k=1}^{K} \mu'_k\phi'_k & \text{(58c)} \\ z = \displaystyle\sum_{j=1}^{J}(-\xi_j\breve{\mu}_j)\phi_j + 2\Re\sum_{k=1}^{K}(-\xi'_k + j\omega'_k)\breve{\mu}'_k\phi_k + \left[G(0) + \sum_{j=1}^{J}\breve{\mu}_j + 2\Re\sum_{k=1}^{K}\breve{\mu}'_k\right] u & \text{(58d)} \end{cases}$$

where z and y are output variables of the considered system, while u is the input variable. The coefficients of this model are obtained by an optimization procedure corresponding to solving a least-square problem with constraint.

5 Comparison of several models

This section is devoted to compare models Zwikker and Kosten (ZK) ("ZK"), Cremer and Viscothermal boundary conditions applied to the linear acoustic equations in a 3D axisymmetric domain (36- 37) ("CR") and (36- 38) ("VI"), and Webster-Lokshin (53) ("WL").

5.1 Domains of validity

In Fig. 10 are sketched the different domains of validity of some models, in the space (frequency, radius), for a cylindrical pipe. Thermoviscous equations come from the linearization of Navier-Stokes equations, and are followed by the assumption that $k/s \ll 1$ to obtain all the following models. Moreover,

- ZK model assumes that $k \ll 1$ (dotted region),
- Webster-Lokshin and Keefe assume that $k \ll 1$ and $s \gg 1$ (horizontally hatched region),
- The sequential linearized NS model as well as 3D Helmholtz equation with efficient boundary conditions assume that $s \gg 1$ (diagonally hatched region).

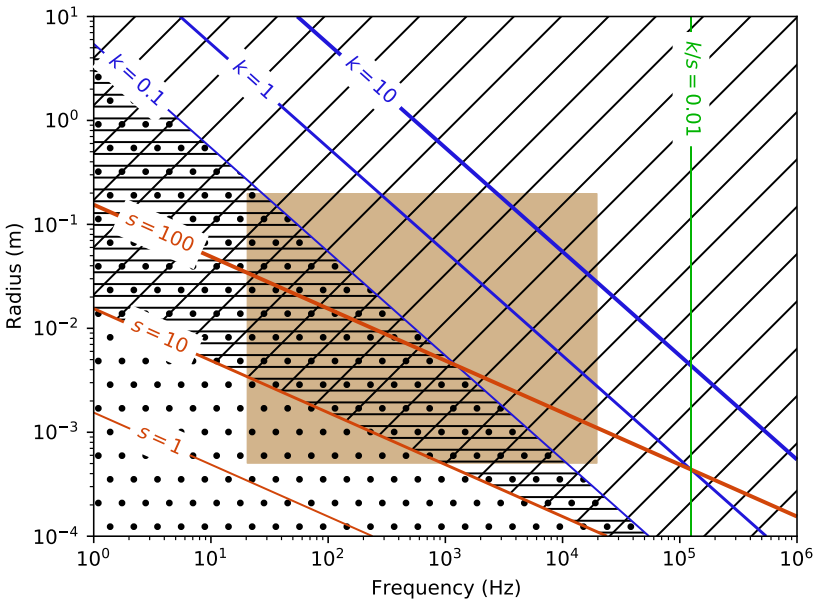

Figure 10: Expected domains of validity of the various models. The filled rectangle represents the range of pipe radii and frequencies of interest in musical acoustics. Curves of constant Stokes number $s = R\sqrt{\rho_0\omega/\mu}$ and reduced frequency $k = R\omega/c_0$ are displayed. The dotted region is where model (ZK) is expected to be valid, according to the hypotheses made. Similarly, Webster–Lokshin and Keefe models should give accurate results in the horizontally hatched region, and the 3D models with efficient boundary conditions should be valid in the region with diagonal hatches.

5.2 Quantitative error on the wavenumber

In Fig 11 are displayed the relative errors on the wavenumber computed from three different models : ZK, Keefe and WL, with respect to the exact one (14). Surprisingly, ZK remains valid for high k, and the error depends mostly on the ratio k/s. Since Keefe is a large-s approximation of ZK, it becomes invalid at low frequencies and pipe radii. As noted in (55), WL can be interpreted as a large-s approximation of lower order than Keefe, thus leading to significant error at low frequencies and pipe radii.

An important observation is the quantitative value of these relative errors in the musical acoustics range in interest (black rectangle). It is smaller than 10^{-4} for ZK, but can exceed 10^{-1} with Keefe and WL models when s is small.

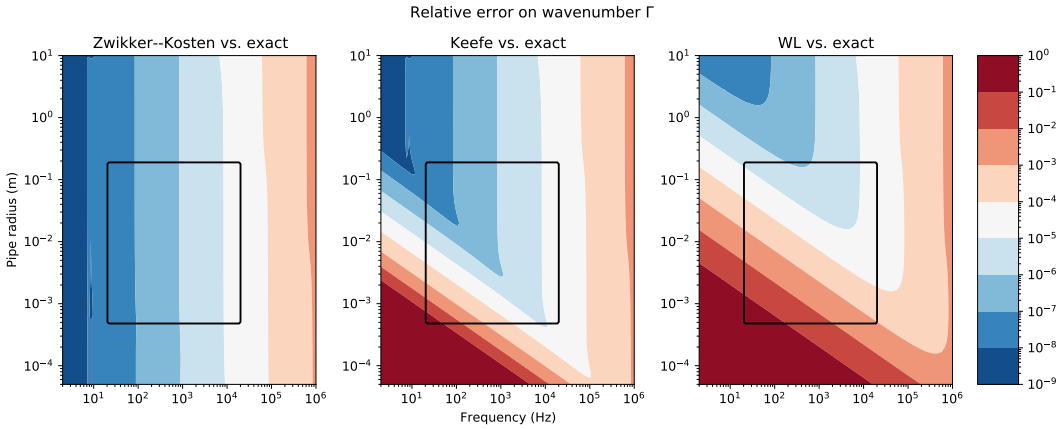

Figure 11: Relative error on the wavenumber, for models ZK, Keefe and WL, comparing them to the exact result (14).

5.3 Cylinder

We use the same cylindrical case as in Sec. 3.3.1: a 20 cm long cylinder with radius 4 mm. In Fig 12 is displayed the modulus (top) and angle (bottom) of the input impedance of the cone between .5 and 8.5 kHz, along with specific chosen values for model comparison. Recall that in the cylinder, Zwikker and Kosten model provides the exact solution to Eq. (16) , which neglects terms $\mathcal{O}(k)$ and $\mathcal{O}(k/s)$ from the thermo-viscous equations. It is therefore considered as the most precise model in this case. Every computations ensures that the solution has reached convergence up to machine precision. In Fig. 13 to 19 are displayed the input impedances in the complex plane (left) computed by solving the four models, and an array of relative errors between these models (right), at 845 Hz, 1 kHz, 2 kHz, 3 kHz, 4 kHz, 6 kHz, and 8 kHz respectively. The values of the impedances are all normalized by the modulus of the ZK solution.

For each frequency, the largest relative error between models is around $0.3 - 3\%$.

For all frequencies it can be noted that two groups of solutions emerge : {ZK and VISCO BC} in hot colors, as opposed to { WL and CREMER BC} in cold colors. The largest relative error almost always occurs between these two groups. By examining the second column of the arrays, we notice that the 3D-axi solution obtained with VISCO BC approaches the ZK solution with a better accuracy than with CREMER BC (the only exception is the computation at 6 kHz where the real part is dominating in the input impedance). Observing the last column of the first row show the very good agreement between the WL and CR models, which was to be expected since WL model is based on the CR effective boundary condition. Since ZK is considered as the most exact solution in the cylindrical case, we conclude that VISCO BC provide a more accurate 3D solution than CREMER BC.

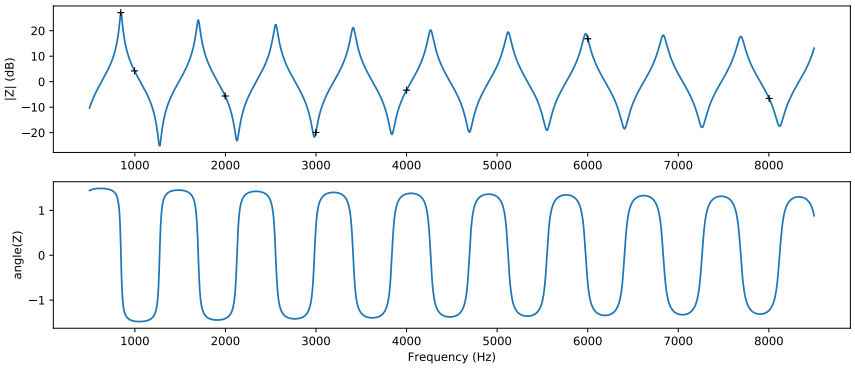

Figure 12: Input impedance of the cylinder. The black crosses show the specific chosen frequencies.

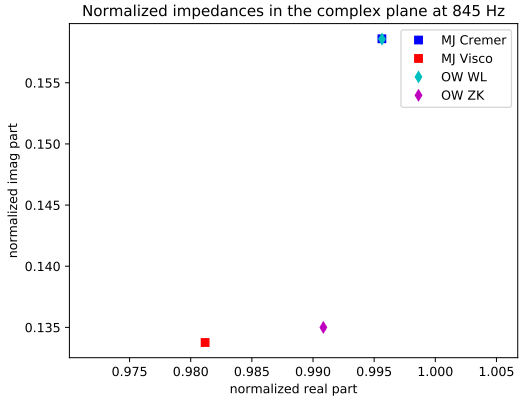

(a) Normalized impedances in the complex plane. At this frequency, the real part is dominating.

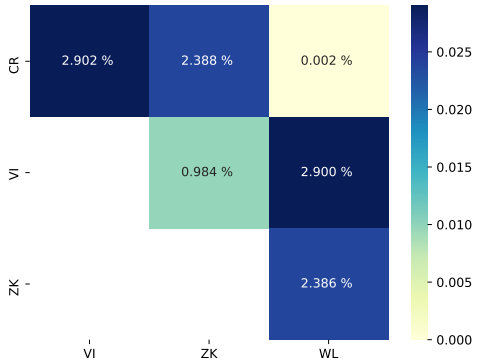

(b) Relative error between the different models

Figure 13: Input impedance of the 20 cm long cylinder of radius 4 mm at 845 Hz computed with various models. The best solution is expected to be given by the ZK model.

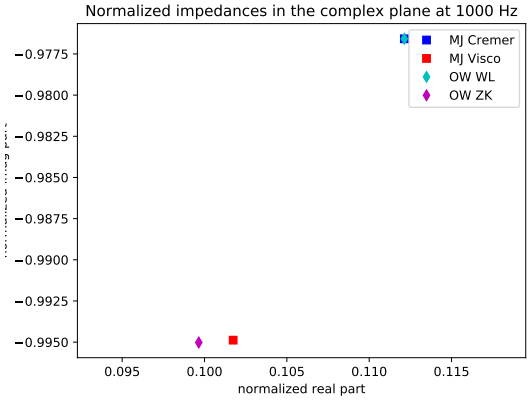

(a) Normalized impedances in the complex plane. At this frequency, the imaginary part is dominating.

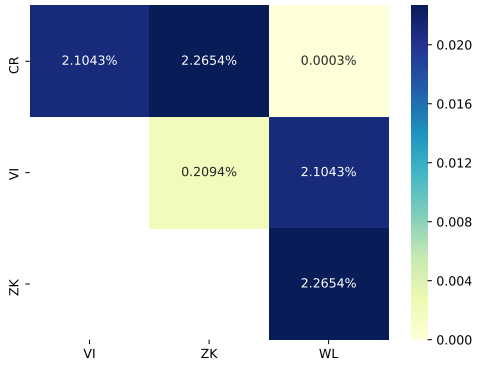

(b) Relative error between the different models

Figure 14: Input impedance of the 20 cm long cylinder of radius 4 mm at 1 kHz computed with various models. The best solution is expected to be given by the ZK model.

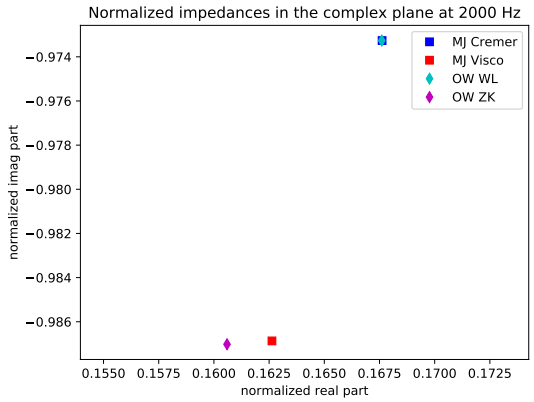

(a) Normalized impedances in the complex plane. At this frequency, the imaginary part is dominating.

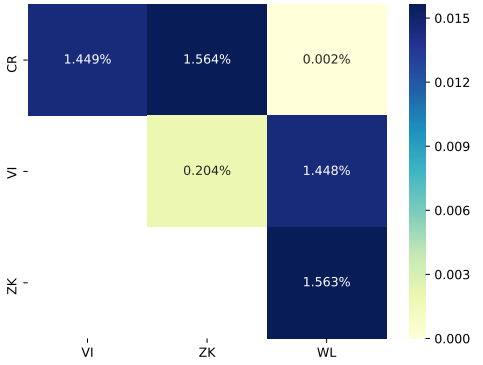

(b) Relative error between the different models

Figure 15: Input impedance of the 20 cm long cylinder of radius 4 mm at 2 kHz computed with various models. The best solution is expected to be given by the ZK model.

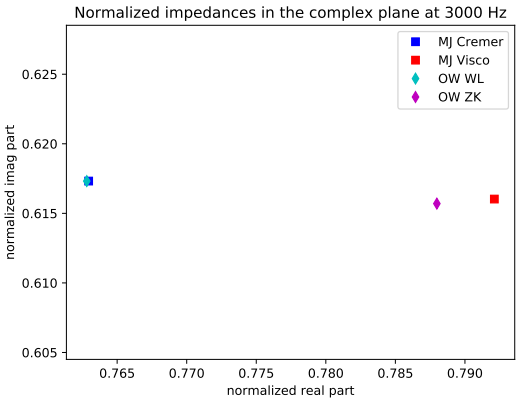

(a) Normalized impedances in the complex plane. At this frequency, the imaginary part and real part are comparable.

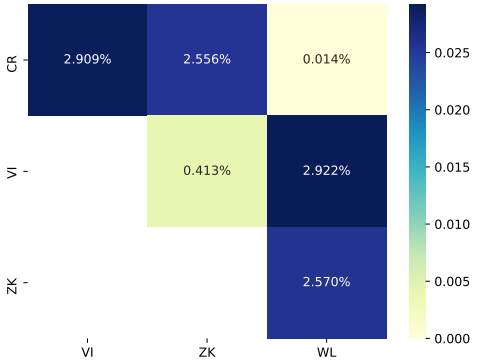

(b) Relative error between the different models

Figure 16: Input impedance of the 20 cm long cylinder of radius 4 mm at 3 kHz computed with various models. The best solution is expected to be given by the ZK model.

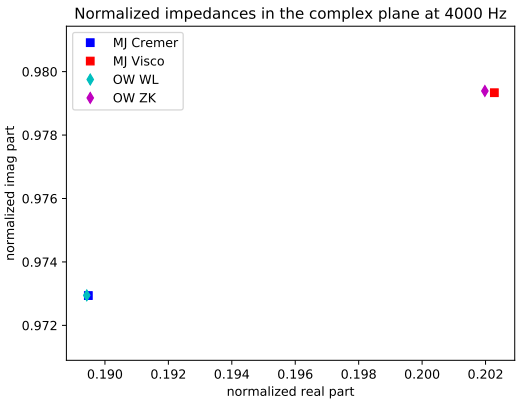

(a) Normalized impedances in the complex plane. At this frequency, the imaginary part is dominating.

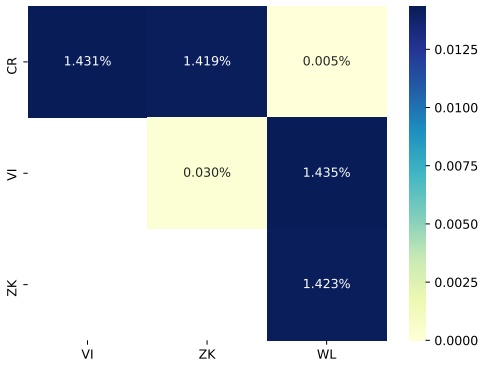

(b) Relative error between the different models

Figure 17: Input impedance of the 20 cm long cylinder of radius 4 mm at 4 kHz computed with various models. The best solution is expected to be given by the ZK model.

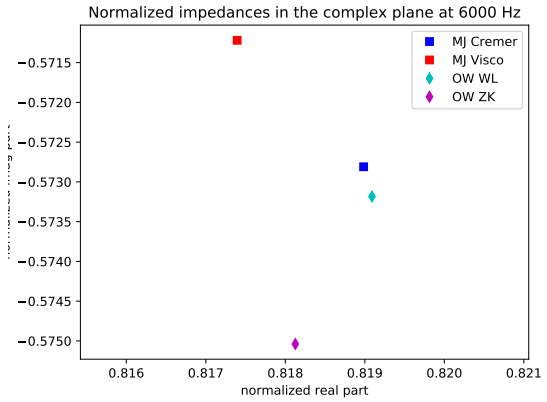

(a) Normalized impedances in the complex plane. At this frequency, the real part is dominating.

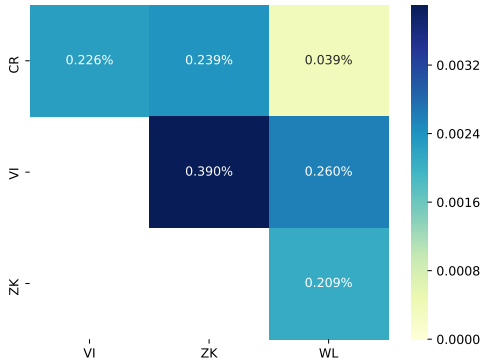

(b) Relative error between the different models

Figure 18: Input impedance of the 20 cm long cylinder of radius 4 mm at 6 kHz computed with various models. The best solution is expected to be given by the ZK model.

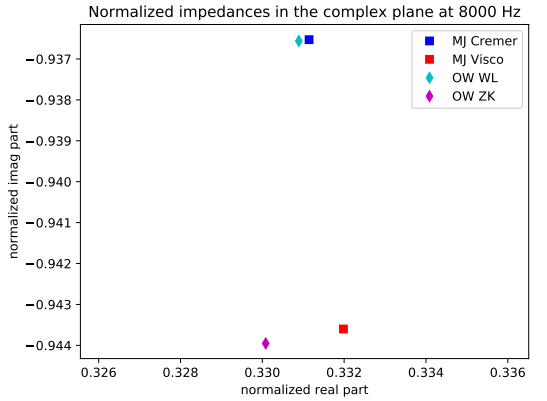

(a) Normalized impedances in the complex plane. At this frequency, the imaginary part is dominating.

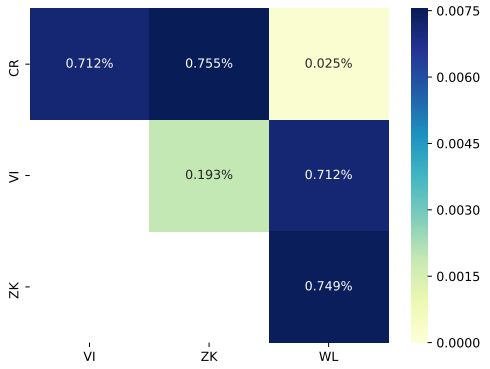

(b) Relative error between the different models

Figure 19: Input impedance of the 20 cm long cylinder of radius 4 mm at 8 kHz computed with various models. The best solution is expected to be given by the ZK model.

5.4 Cone

We use the same conical cas as in Sec. 3.3.2. No analytical solutions to equations are available for this case. In Fig 20 is displayed the modulus (top) and angle (bottom) of the input impedance of the cone between .5 and 2.5 kHz, along with four specific chosen values for models comparison.

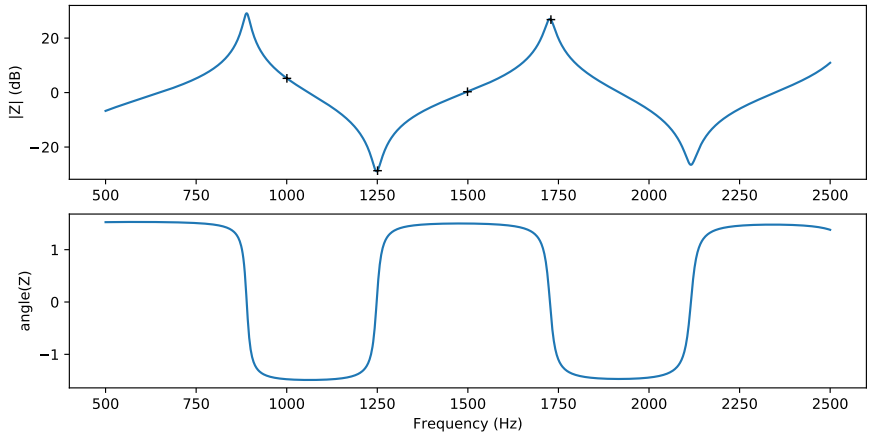

Figure 20: Input impedance of the cone. The black crosses show the specific chosen frequencies.

In Fig. 21 are displayed the input impedances in the complex plane computed by solving the four models. The values of the impedances are all normalized by the modulus of the ZK solution. In circles and squares are displayed the impedances computed with Montjoie software that solves the 3D (axi) acoustic with specific boundary conditions CREMER BC (blue) and VISCO BC (red). In diamonds are displayed the impedances computed with OpenWind that solves the 1D models ZK (red) and WL (blue). In red triangles are displayed the impedances computed with the diffusive representation with $M = 8$ described in Sec. 4.5.1. Each simulation is run twice, without (filled markers) and with (empty markers) the spherical geometry of exterior surfaces that force spherical waves (see Sec. 3.3.2 for the explanation of spherical waves in 3D configurations). Every computations ensures that the solution has reached convergence up to machine precision.

In Fig. 22 are displayed arrays of relative errors between these models using planar (left) or spherical (right) waves, at 1 kHz, 1.25 kHz, 1.5 kHz and 1.73 kHz respectively. The 3D models are considered using the conical adaptation piece and respectively planar or spherical input and output surfaces.

In this conical case, as in the cylindrical case, for all frequencies it can be noted that two groups of solutions emerge : {ZK and VISCO BC} in red, as opposed to { WL and CREMER BC} in blue. The largest relative error, which lies in $0.5 - 5\%$, almost always occurs between these two groups.

One first observation is that for planar 3D models (ie with planar in and out surfaces), both cylindrical and conical adaptation geometries give a very similar input impedance (filled circle and filled square), for CREMER (blue) and VISCO (red) boundary conditions. On the other hand, when providing spherical in and out surfaces, the choice of adaptation geometry (cylindrical or conical) greatly influences the result, for CREMER (blue) and VISCO (red) boundary conditions.

A second observation is that the 1D ZK models are close to the 3D VISCO BC models in spherical and planar configurations with conical adaptation piece, while the 1D WL models are close to the 3D CREMER BC models in spherical and planar configurations with conical adaptation piece. This observation is interesting since for the conical case, ZK is not *a priori* a best 1D solution than WL, but it is however closer to the 3D VISCO BC which showed to provide a more complete model than CREMER BC in the previous section (cylindrical case). This preliminary result should be confirmed by other numerical tests, especially in cases where the pipe radius varies continuously.

Finally, it can be observed that the diffusive representation is closest to ZK than any other model, showing that the error model of the diffusive representation with $M = 8$ is small with respect to the other observed model errors between hereby considered models (1D and 3D).

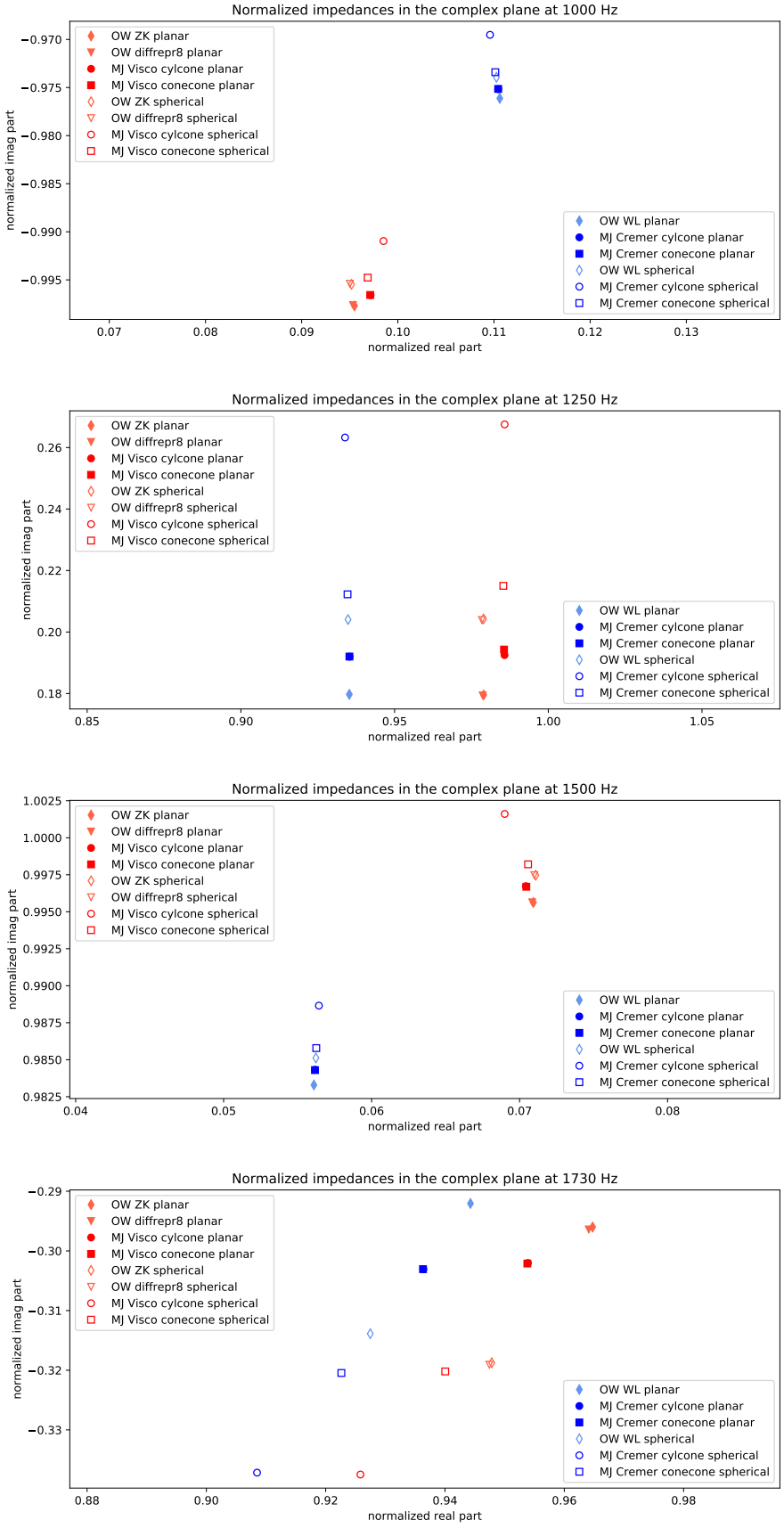

Figure 21: Input impedance of a cone at frequencies 1 kHz, 1.25 kHz, 1.5 kHz and 1.73 kHz. Comparison of several models. Models of planar waves are associated with filled markers, models of spherical waves with empty markers.

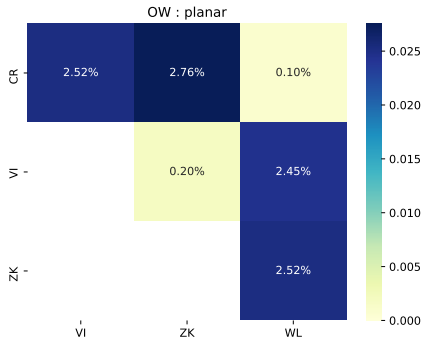

(a) Planar waves, 1 kHz

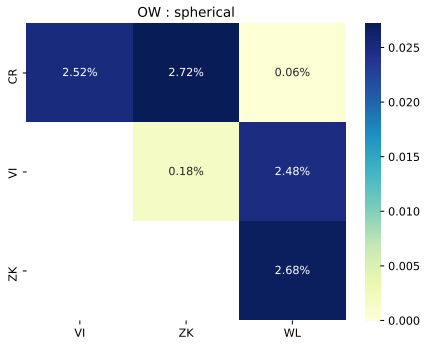

(b) Spherical waves, 1 kHz

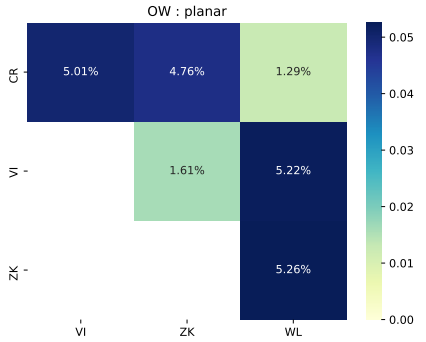

(c) Planar waves, 1.25 kHz

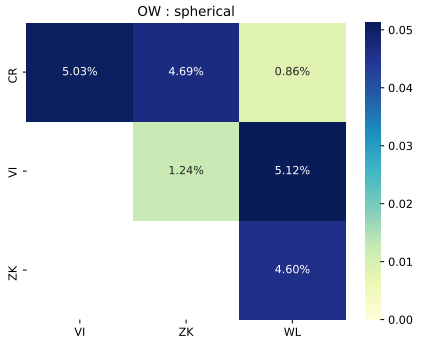

(d) Spherical waves, 1.25 kHz

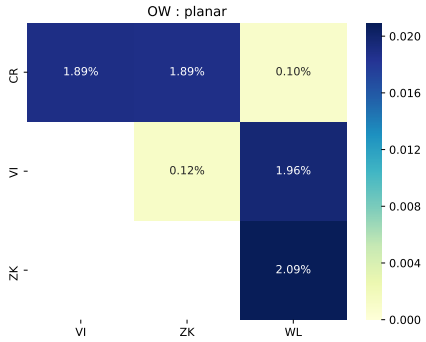

(e) Planar waves, 1.5 kHz

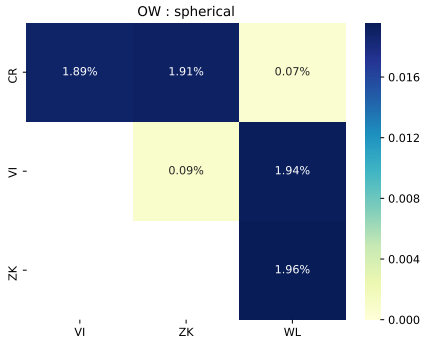

(f) Spherical waves, 1.5 kHz

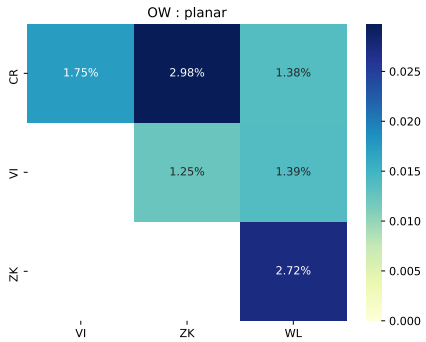

(g) Planar waves, 1.73 kHz

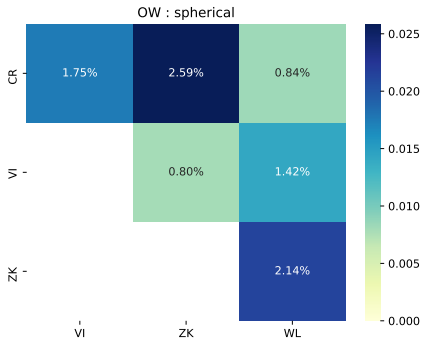

(h) Spherical waves, 1.73 kHz

Figure 22: Relative error between input impedance of a cone at frequencies 1 kHz, 1.25 kHz, 1.5 kHz and 1.73 kHz. Comparison of several models.

6 Conclusions

Different models of viscothermal effects on linear wave propagation in pipes have been recalled, derived, assessed and compared. The underlying hypotheses and assumptions have been specified and quantified in Fig. 10. 3D models with equivalent boundary conditions (that model the presence of viscous and thermal boundary layers) have been compared with various 1D models as Zwikker-Kosten and Webster-Lokshin. The errors between models differ as the regime changes, however, is ranges between 2×10^{-3} and 5 % for the considered cases. This error is expected to grow as the underlying assumptions are violated, mostly as the Stokes number s diminishes (low frequencies, thin pipes). No analytical solution is available for any given geometry, therefore conclusions can not be drawn a priori from these comparisons. Implementing the thermoviscous equations and using them as a reference model should help in the finer assessment of the models errors.

References

[Bareau and Pagneux,] Bareau, L. and Pagneux, V. Analyse des trois familles de modes de propagation en guide d'onde cylindrique: applicationa l'étude de discontinuités.

[Berggren et al., 2018] Berggren, M., Bernland, A., and Noreland, D. (2018). Acoustic boundary layers as boundary conditions. Journal of Computational Physics, 371:633 – 650.

[Bilbao and Chick, 2013] Bilbao, S. and Chick, J. (2013). Finite difference time domain simulation for the brass instrument bore. The Journal of the Acoustical Society of America, 134(5):3860–3871.

[Bilbao and Harrison, 2016] Bilbao, S. and Harrison, R. (2016). Passive time-domain numerical models of viscothermal wave propagation in acoustic tubes of variable cross section. The Journal of the Acoustical Society of America, 140(1):728–740.

[Bilbao et al., 2015] Bilbao, S., Harrison, R., Kergomard, J., Lombard, B., and Vergez, C. (2015). Passive models of viscothermal wave propagation in acoustic tubes. The Journal of the Acoustical Society of America, 138(2):555–558.

[Bossart et al., 2003] Bossart, R., Joly, N., and Bruneau, M. (2003). Hybrid numerical and analytical solutions for acoustic boundary problems in thermo-viscous fluids. Journal of Sound and Vibration, 263(1):69–84.

[Bruneau, 2013] Bruneau, M. (2013). Fundamentals of acoustics. John Wiley & Sons.

[Bruneau et al., 1989] Bruneau, M., Herzog, P., Kergomard, J., and Polack, J. (1989). General formulation of the dispersion equation in bounded visco-thermal fluid, and application to some simple geometries. Wave motion, 11(5):441–451.

[Chaigne and Kergomard, 2016] Chaigne, A. and Kergomard, J. (2016). Acoustics of musical instruments. Springer.

[Cremer, 1948] Cremer, L. (1948). On the acoustic boundary layer outside a rigid wall. Arch. Elektr. Uebertr, 2:235.

[Ernoult and Kergomard, 2020] Ernoult, A. and Kergomard, J. (2020). Transfer matrix of a truncated cone with viscothermal losses: application of the wkb method.

[Hélie et al., 2013] Hélie, T., Hézard, T., Mignot, R., and Matignon, D. (2013). One-dimensional acoustic models of horns and comparison with measurements. Acta acustica united with Acustica, 99(6):960–974.

[Hélie and Matignon, 2006] Hélie, T. and Matignon, D. (2006). Diffusive representations for the analysis and simulation of flared acoustic pipes with visco-thermal losses. Mathematical Models and Methods in Applied Sciences, 16(04):503–536.

[Jith and Sarkar, 2018] Jith, J. and Sarkar, S. (2018). Boundary layer impedance model to analyse the visco-thermal acousto-elastic interactions in centrifugal compressors. Journal of Fluids and Structures, 81:179–200.

[Joly, 2010] Joly, N. (2010). Finite element modeling of thermoviscous acoustics on adapted anisotropic meshes: Implementation of the particle velocity and temperature variation formulation. Acta acustica united with acustica, 96(1):102–114.

[Kampinga et al., 2010] Kampinga, W., Wijnant, Y. H., and de Boer, A. (2010). Performance of several viscothermal acoustic finite elements. Acta acustica united with Acustica, 96(1):115–124.

[Kampinga et al., 2011] Kampinga, W., Wijnant, Y. H., and de Boer, A. (2011). An efficient finite element model for viscothermal acoustics. Acta Acustica united with Acustica, 97(4):618–631.

[Keefe, 1984] Keefe, D. H. (1984). Acoustical wave propagation in cylindrical ducts: Transmission line parameter approximations for isothermal and nonisothermal boundary conditions. The Journal of the Acoustical Society of America, 75(1):58–62.

[Kirchhoff, 1868] Kirchhoff, G. (1868). Ueber den einfluss der wärmeleitung in einem gase auf die schallbewegung. Annalen der Physik, 210(6):177–193.

[Lefebvre and Scavone, 2010] Lefebvre, A. and Scavone, G. (2010). Finite element modeling of woodwind instruments. In Proceedings of 20th International Symposium on Music Acoustics, pages 215–222.

[Lefebvre et al., 2013] Lefebvre, A., Scavone, G. P., and Kergomard, J. (2013). External tonehole interactions in woodwind instruments. Acta Acustica united with Acustica, 99(6):975–985.

[Malinen et al., 2004] Malinen, M., M, L., P, R., A, K., and L, K. (2004). A finite element method for the modeling of thermo-viscous effects in acoustics. In Proceedings of the European Congress on Computational Methods in Applied Science and Engineering (ECCOMAS 2004).

[Regev et al., 2016] Regev, O., Umurhan, O. M., and Yecko, P. A. (2016). Modern Fluid Dynamics for Physics and Astrophysics. Springer.

[Rienstra, 2005] Rienstra, S. W. (2005). Webster's horn equation revisited. SIAM Journal on Applied Mathematics, 65(6):1981–2004.

[Schmutzhard et al., 2017] Schmutzhard, S., Chatziioannou, V., and Hofmann, A. (2017). Parameter optimisation of a viscothermal time-domain model for wind instruments. In Proceedings of the 2017 International Symposium on Musical Acoustics, pages 27–30.

[Stinson, 1991] Stinson, M. R. (1991). The propagation of plane sound waves in narrow and wide circular tubes, and generalization to uniform tubes of arbitrary cross-sectional shape. The Journal of the Acoustical Society of America, 89(2):550–558.

[Thompson et al., 2014] Thompson, S. C., Gabrielson, T. B., and Warren, D. M. (2014). Analog model for thermoviscous propagation in a cylindrical tube. The Journal of the Acoustical Society of America, 135(2):585–590.

[Tijdeman, 1975] Tijdeman, H. (1975). On the propagation of sound waves in cylindrical tubes. Journal of Sound and Vibration, 39(1):1–33.

[Tournemenne and Chabassier, 2019] Tournemenne, R. and Chabassier, J. (2019). A comparison of a one-dimensional finite element method and the transfer matrix method for the computation of wind music instrument impedance. Acta Acustica united with Acustica, 105(5):838–849.

[Zwikker and Kosten, 1949] Zwikker, C. and Kosten, C. W. (1949). Sound Absorbing Materials. Elsevier Publ. Comp.

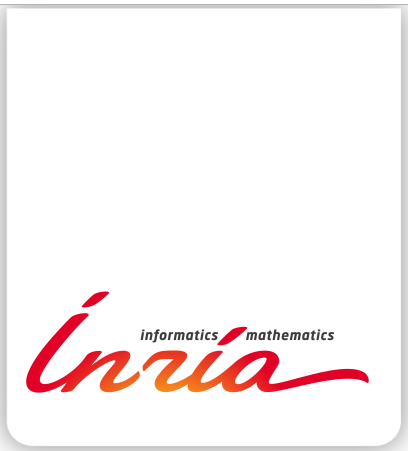

RESEARCH CENTRE
BORDEAUX – SUD-OUEST

200 Avenue de la Vieille Tour,
33405 Talence Cedex

Publisher
Inria
Domaine de Voluceau - Rocquencourt
BP 105 - 78153 Le Chesnay Cedex
inria.fr

ISSN 0249-6399